ORNL/TM-2019/1206
CRADA/NFE-16-06412

Level-set Modeling Simulations of Chemical Vapor Infiltration for Ceramic Matrix Composites Manufacturing

OAK RIDGE NATIONAL LABORATORY
MANAGED BY UT BATTELLE
FOR U.S. DEPARTMENT OF ENERGY

Ramanan Sankaran (ORNL)
Vimal Ramanuj (ORNL)
Chong M. Cha (RRC)
David Liliedahl (RRC)

**Approved for public release.
Distribution is unlimited.**

August 21st 2019

OAK RIDGE NATIONAL LABORATORY
MANAGED BY UT-BATTELLE FOR THE US DEPARTMENT OF ENERGY

DOCUMENT AVAILABILITY

Reports produced after January 1, 1996, are generally available free via US Department of Energy (DOE) SciTech Connect.

Website: `http://www.osti.gov/scitech/`

Reports produced before January 1, 1996, may be purchased by members of the public from the following source:

National Technical Information Service
5285 Port Royal Road
Springfield, VA 22161
Telephone: 703-605-6000 (1-800-553-6847)
TDD: 703-487-4639
Fax: 703-605-6900
E-mail: info@ntis.gov
Website: `http://classic.ntis.gov/`

Reports are available to DOE employees, DOE contractors, Energy Technology Data Exchange representatives, and International Nuclear Information System representatives from the following source:

Office of Scientific and Technical Information
PO Box 62
Oak Ridge, TN 37831
Telephone: 865-576-8401
Fax: 865-576-5728
E-mail: report@osti.gov
Website: `http://www.osti.gov/contact.html`

This report was prepared as an account of work sponsored by an agency of the United States Government. Neither the United States Government nor any agency thereof, nor any of their employees, makes any warranty, express or implied, or assumes any legal liability or responsibility for the accuracy, completeness, or usefulness of any information, apparatus, product, or process disclosed, or represents that its use would not infringe privately owned rights. Reference herein to any specific commercial product, process, or service by trade name, trademark, manufacturer, or otherwise, does not necessarily constitute or imply its endorsement, recommendation, or favoring by the United States Government or any agency thereof. The views and opinions of authors expressed herein do not necessarily state or reflect those of the United States Government or any agency thereof.

ORNL/TM-2019/1206
CRADA/NFE-16-06412

Level-set Modeling Simulations of Chemical Vapor Infiltration for Ceramic Matrix Composites Manufacturing

Ramanan Sankaran and Vimal Ramanuj
Oak Ridge National Laboratory (ORNL)

Chong M. Cha and David Liliedahl
Rolls-Royce Corporation (RRC)

Date Published: August 21st 2019

Prepared by
OAK RIDGE NATIONAL LABORATORY
Oak Ridge, TN 37831-6283
managed by
UT-Battelle, LLC
for the
US DEPARTMENT OF ENERGY
under contract DE-AC05-00OR22725

CONTENTS

LIST OF FIGURES v
ACKNOWLEDGEMENTS vii
ABSTRACT 1
1. INTRODUCTION 2
2. IMPACT 4
3. PHYSICAL MODEL 4
4. NUMERICAL METHOD 6
  4.1 Level Set Method 7
    4.1.1 Anchoring at the bounding nodes 9
    4.1.2 Solving at the interior nodes 10
  4.2 Immersed Boundary Method 11
  4.3 Diffusion Solver 13
  4.4 Level Set Initialization 14
  4.5 Preform Geometry Assembly 16
  4.6 Code Description 18
5. RESULTS AND DISCUSSION 19
  5.1 Modeling of the structure functions 20
  5.2 Modeling of flow infiltration 28
6. FUTURE WORK 32

LIST OF FIGURES

1 Two limiting (unoptimized) chemical vapor infiltration processes. 3
2 Schematic of the Cartesian mesh showing location of interface 8
3 Schematic of three point upwind finite difference stencils for fast sweeping method. 11
4 A standard second order central difference stencil at a grid point near an immersed interface 12
5 Immersed boundary formulation using level set information 13
6 Example configuration showing possibilities for the shortest distance of a point from a triangulated surface 15
7 Transformation of a triangulated plain weave to a level set function on a structured mesh . . 16
8 Fiber resolved geometry of a 5 layered 5hs weave. 17
9 Single layer of a 5hs weave consisting of five warp-weft pairs. 17
10 A warp-weft pair in a 5hs weave 18
11 Translation of triangles in a bundle of fibers 18
12 Methodology to initialize level set function (LSF) on a structured mesh for a fiber resolved layered 5hs preform from a single triangulated fiber bundle. 19
13 Partially-densified woven preforms from the DNS simulations. 21
14 Cross-sections of the initial and final preform for the $K = 1 \times 10^{-3}$ case. 22
15 Cross-sections of the initial and final preform for the $K = 1 \times 10^{-1}$ case. 23
16 Illustration of DNS simulations for a fiber-resolved case. 24
17 Surface area dependence on porosity and Thiele modulus. 27
18 Steady-state pressure field used to compute weave permeability. 29
19 Inert species concentrations used to compute effective diffusivity. 29
20 Permeability and effective diffusivity scaling with porosity. 31
21 Proportionality of permeability to effective diffusivity. 32

ACKNOWLEDGEMENTS

This research was supported by the High-Performance Computing for Manufacturing Project Program (HPC4Mfg), managed by the U.S. Department of Energy Advanced Manufacturing Office (AMO) within the Energy Efficiency and Renewable Energy Office (EERE). It was performed using resources of the Oak Ridge Leadership Computing Facility (OLCF) and Oak Ridge National Laboratory, which are supported by the Office of Science of the U.S. Department of Energy under Contract No. DE-AC0500OR22725.

ABSTRACT

Silicon-carbide (SiC) reinforced ceramic matrix composites (CMCs) are a key enabling technology to reduce fuel consumption and emissions of gas turbine engines. In one manufacturing approach, chemical vapor infiltration (CVI) is limited to only coating SiC fibers. The preform is then fabricated using a lay-up of basic plys or 2-D woven sheets composed of the precoated fibers. At the other extreme, CVI is used to completely densify a 3-D woven preform shaped almost like the gas turbine component itself. The latter approach is more suitable for highly engineered components which sit directly in the gas path of the engine, for example, a high pressure turbine blade. In this case, the geometry is necessarily complex for aerodynamic, stress, and lifing (multi-physics) requirements. Presently, optimizing the CVI-dominated manufacturing approach is largely by trial-and-error. In this work, a first-principles modeling of CVI is performed to realize optimization of SiC/SiC CMC manufacturing.

The modeling is based on a level-set framework to describe the interface between the vapor and solid phases. A finite-difference numerical scheme using an immersed boundary method is developed for fixed, structured meshes. Massively parallel direct numerical simulations (DNS) of CVI through fiber-woven geometries are performed using one-step chemistry, and over a range of Thiele moduli. Illustrative applications of the resulting large DNS data sets are given, including the development of fiber-weave specific infiltration models and structure functions for mean-field (porous media) Computational Fluid Dynamics (CFD) simulations of CVI.

1. INTRODUCTION

Materials processing by Chemical Vapor Deposition (CVD) is fundamental in advancing materials fabrication for semiconductor, microelectronic, optics, nuclear, friction (brakes), and propulsion applications. For example, in the gas turbine industry, silicon-carbide (SiC) reinforced ceramic matrix composites (CMCs) offer higher strength and temperature capability over metal super-alloys at a significantly reduced weight. CMCs are thus currently a key enabling technology to realize the reduced fuel consumption and lower emissions necessary to sustain the continual, rapid growth in the air transportation industry.

In one CMC manufacturing approach, CVD is used to densify a complex three-dimensional preform of the entire engineered component. Optimizing this manufacturing approach is largely by trial-and-error presently. The primary challenge stems from the need of the chemical vapor species to completely infiltrate and egress from an evolving, complex network of channels. This fluid network is initially characterized by the preformed geometry, or simply, "preform" of the engineered component. Fibers (each typically of order 10 μm in diameter) are collected into bundles (around 1 mm in diameter) and woven to construct the preform (around 10 cm or larger). The initial preform is mostly void of the solid (fiber) material. The desired material properties of the final processed components are governed by the initial preform geometry and the final porosity, uniformity, and chemical makeup of the matrix material that has deposited on the preform by heterogeneous chemical reactions. Although Reynolds numbers are low in Chemical Vapor Infiltration (CVI) processing, the problem requires a large range of scales (around 10^5) to be resolved due to the micro-scale structure of the geometry.

The optimization issues of the CVI process are illustrated in Fig. 1 which shows a region near the manufactured part boundary under two different processing conditions. The dark blue circles represent the preform geometry, the deposited solid matrix material (SiC) is in grey, and the surrounding colors show the concentration of the precursor vapor species. The highest concentrations are red, lowest in blue. Here, the precursor vapor diffuses into the preform from above. Plot (a) illustrates an unoptimized process where, for example, the uniform furnace temperature is too low making SiC deposition slow with respect to the transport of the precursor vapor. However, the result is good, uniform growth in the matrix throughout the part, but at the costly expense of a long manufacturing time. In plot (b), the furnace temperature has been increased, increasing the SiC deposition rate. (Due to the governing Arrhenius kinetics, the chemical timescale is much more sensitive to temperature than diffusion.) As a result, at the same processing time as in (a), the relatively fast matrix growth just on the surface of part (b) creates a large, vacuous region that can no longer be infiltrated by the precursor gases, an "inaccessible pore". Such pore closures can occur anywhere in the preform. Such porosity of the CMC adversely affects both its material strength and thermal properties. The reduction in quality due to the porosity reduces manufacturing part yield, which is costly.

The objectives of this work is to perform three-dimensional numerical simulations that: (i) capture complex geometry (the initial complex preform geometry and the changing topology due to local and time-dependent deposition rate), and (ii) couple the evolving geometry to the transport of precursor species and a given description of the chemical kinetics. Both of these objectives are required at a minimum to address the optimization problem. The level-set approach, described in detail in Section 4 is used to address (i). A simple one-step kinetic model of the form,

$$\text{Gaseous Reactant} \longrightarrow \text{Surface Deposit} + \text{Gaseous Product} \qquad (1)$$

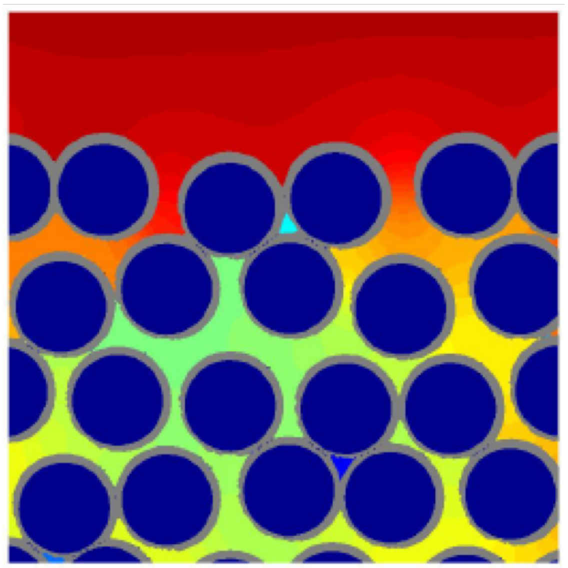

(a) Slow deposition

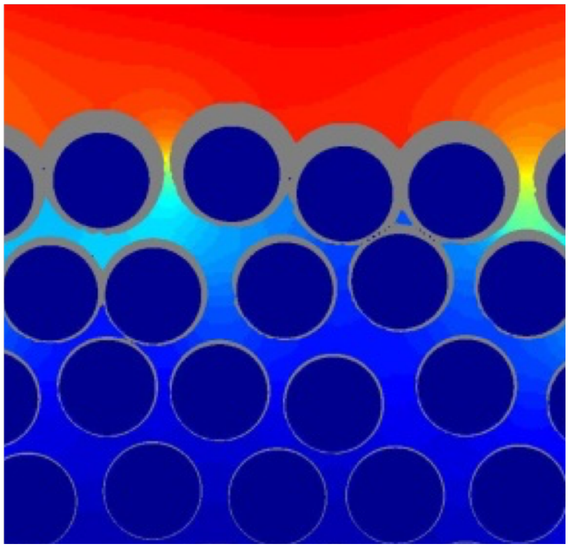

(b) Fast deposition

Figure 1. Two limiting (unoptimized) chemical vapor infiltration processes. In (a), the chemical timescale is much larger than the transport of vapor. In (b), the chemical timescale is relatively much smaller.

is adopted for (ii). The simulations were performed with Quilt, a massively parallel porous media reacting flow solver using the high performance computing (HPC) resources at ORNL.

2. IMPACT

The market for aircraft gas turbine engines was $60 Billion in 2015 and continues to increase due to the ever-increasing demand for air transportation, estimated to double in the next decade. While this is a major economic opportunity for this specific U.S. manufacturing sector, reduced fuel consumption and lower emissions must first be met for this trend to be sustainable.

The high temperature capability of CMCs allow for reducing cooling air needs for turbine engine components thus increasing turbine efficiency. The improved turbine efficiency reduces the specific fuel consumption (SFC) of the engine. The reduced weight of CMC components for the combustor and turbine also reduce SFC directly and allow for lighter supporting structures, further reducing total SFC. Total savings in SFC alone are estimated to be around 10%. The dollar value of this SFC reduction is significant given that fuel costs are the largest fraction by far of a civil airliner's direct operating costs (roughly 25% compared to the second highest of 15% for maintenance). A reduction in SFC also directly reduces CO2 emissions and allows for reduced NOx due to turbine cooling air savings that can be exploited by the combustor. The level of NOx reduction depends upon combustor design, but could allow already technologically mature (rich-burn) redesigns to meet International Civil Aviation Organization targets.

The manufacturing of CMCs by CVI processing is very expensive because it is slow, involves large volumes of chemicals (some of which are explosive or hazardous), and is performed at extreme operating conditions (low pressures and high temperatures). Currently, the manufacturing of CMC components by CVI can take on the order of weeks. Even a small reduction in this time will greatly impact reduction in the manufacturing costs. An ability to optimize the CVI process for non-oxide (SiC/SiC) CMCs will also read across to other industries, such as carbon/carbon brake manufacturing and the nuclear power industry.

The important advantages of CVI still motivate the pursuit of this manufacturing route in spite of the resulting high expense. Presently, CVI processing has largely been optimized by trial-and-error due to its high complexity. The optimization of CVI will be accelerated by the simulation methodology developed here, which allows the porous structure evolution of the preform densification to be known. The high resolution simulations that resolve the weave microstructure, which constitutes a direct numerical simulation (DNS) of the porous media microstructure, can only be realized with state-of-art HPC resources. The primary role of this project was to validate and demonstrate the weave resolving simulations of CVI. The computational tool along with HPC resources will allow a much cheaper, virtual method of evaluating, for example, optimized fiber weave geometries, to reduce CVI manufacturing time. Another important impact of the DNS will be to develop or help improve fit-for-purpose porous media modeling of CVI fiber weave preforms for more computationally tractable, mean-field modeling and simulation of CVI processing.

3. PHYSICAL MODEL

Chemical vapor infiltration in a porous media is a complex interplay of several physical and chemical phenomena involving the species transport, temperature distribution, gas phase and surface chemical reactions, deposition of solid on the preform, and the change in porous media topology due to the deposition. The physical and chemical models employed along with the assumptions made are listed below.

- The convection of reactant gases within the infiltration reactor can create a temperature and concentration profile based on the local convective and radiative effects. In this work, we assume that the concentrations are uniform at a finite distance away from the preform. We also assume that the temperature is uniform across the preform thickness.
- The three-dimensional simulations will be performed using periodic boundary conditions in the two directions parallel to the weave. As a result, the transport of reactants through the lateral boundaries of the preform are ignored and only the transport normal to the weave is considered.
- An idealized geometry is used to represent the weave. In the tow resolved simulations, the bundle of fibers constituting a tow are idealized as an impermeable surface. In the fiber resolved simulations, the geometry is modeled as a bundle of 50 impermeable fibers, where the fibers remain approximately parallel to each other for the entire length of a tow.
- The present simulations consider diffusive transport of the species through the preform without bulk advection. The former is representative of isothermal CVI, while the latter would be important in forced flow CVI.
- The gas phase reactants are modeled using a single scalar, C. The scalar, C, behaves as a progress variable such that C is linearly proportional to the mass fraction of the reactant.

  Let Y_{R} be the mass fraction of the reactant R and any point in the domain. Then $C = Y_{\mathrm{R}}/Y_{\mathrm{R,u}}$, where $Y_{\mathrm{R,u}}$ is the mass fraction of R in the farfield away from the preform. C is unity at the far field and is zero when all of the reactants have been consumed.
- The molecular diffusivity of the reactant, D, is assumed to be constant.
- The system is assumed to be in a pseudo-steady state, such that the time scales of the interface motion over a representative length scale, such as the tow width, is much longer than the timescales of thermal diffusion over the same length. Therefore, the simulation is performed using an operator splitting strategy where the interface motion is updated alternately with the solution of the steady state diffusion equation.

Based on the above assumptions, we derive the following non-dimensional governing equations for the CVI problem. The reaction rate of the one step kinetic model shown in Eq. 1 is taken to be

$$\dot{\omega}_{\mathrm{s}} = AC \exp\left(-T_{\mathrm{A}}/T\right) \quad , \tag{2}$$

where $\dot{\omega}_{\mathrm{s}}$ is the deposition rate of the solid matrix and has the units $\mathrm{kg}/(\mathrm{m}^2 - s)$. In the above, the reaction rate has been modeled using an Arrhenius rate expression, where A is the pre-exponential constant of the Arrhenius rate expression, C is the non-dimensional mass fraction of the reactant, T_{A} is the activation temperature, and T is the temperature. Note, that we have assumed a first order dependence of the reaction rate on the mass fraction of the reactant. A mass balance for the scalar mass fraction of the gaseous reactant on the surface is

$$\frac{D}{l_{\mathrm{ref}}} \frac{\partial C}{\partial n} = \frac{\dot{\omega}_{\mathrm{s}}}{\rho} \quad . \tag{3}$$

Here D is the mass diffusivity of the gaseous reactant, n is the non-dimensional normal coordinate on the interface, ρ is the gas density and l_{ref} is a reference length scale.

The non-dimensional Thiele modulus can be derived as the ratio of the diffusive time scale to the chemical time scale as,

$$K = \frac{A \exp\left(-T_\mathrm{A}/T\right) l_\mathrm{ref}}{\rho D} \ . \tag{4}$$

Then, Eq. 3 becomes,

$$\frac{\partial C}{\partial n} = KC \ . \tag{5}$$

The governing equation for the diffusive transport of the scalar C in the domain, assuming constant diffusivity, is

$$\nabla^2 C = 0 \ , \tag{6}$$

and is subject to the boundary condition in Eq. 5 on the interface. Also, $C = 1$ at the farfield boundaries.

The interface between the solid and the gas is defined using a level set function φ, such that the isosurface $\varphi = 0$ defines the interface. The interface growth is captured by advancing the level set function in time. The velocity with which the interface moves is determined by the deposition rate and the density of the solid matrix. The dimensional speed is given by $\dot{\omega}_\mathrm{s}/\rho_\mathrm{s}$. We define a reference velocity scale, $u_\mathrm{ref} = A \exp\left(-T_\mathrm{A}/T\right)/\rho_\mathrm{s}$, such that the non-dimensional velocity at the interface, $\varphi = 0$, is $S = C$. As is customary in the level set methods, the interface velocity is then propagated throughout the domain, such that it satisfies

$$\nabla S \cdot \nabla \varphi = 0 \ , \tag{7}$$

subject to the boundary condition $S = C$ at $\varphi = 0$. The computed velocity S is used to advance the level set function using

$$\frac{\partial \varphi}{\partial \tau} + S \left|\nabla \varphi\right| = 0 \ , \tag{8}$$

where τ is the non-dimensional time. The reference time scale was defined using l_ref and u_ref as

$$t_\mathrm{ref} = \frac{l_\mathrm{ref}}{u_\mathrm{ref}} = \frac{l_\mathrm{ref}\rho_\mathrm{s}}{A \exp\left(-T_\mathrm{A}/T\right)} = \frac{l_\mathrm{ref}^2}{D}\frac{\rho_\mathrm{s}}{\rho K} \ . \tag{9}$$

Note that the reference time scale is inversely proportional to the Thiele modulus K.

4. NUMERICAL METHOD

The major challenges encountered in the numerical modeling of the governing physics are interface tracking and application of a reactive boundary condition on the advancing front. Interface tracking finds applications in multiple scientific domains including phase transformations and multiphase fluid dynamics to model moving fronts. In the present work, a similar approach has been chosen for modeling deposition resulting from chemical reaction on a surface. The model is also used to apply boundary conditions on the surface required to solve for the transport of the reactive scalar. The method is briefly introduced here along with its numerical implementation. Later, an algorithm for initialization of a layered weave preform on a structured mesh is also shown. It will be used as an initial condition for the transient CVI simulations.

Interface tracking methods are broadly classified as particle/marker based approach and continuum approach. In the former approach, a collection of markers or massless particles represent the front which are transported with interface velocity [1, 2]. Key aspects of this method are the transformation of continuum velocity from Eulerian mesh to Lagrangian particles. Interface reconstruction can be achieved by connecting the markers, such as through high order polynomials. However, special care must be exercised to maintain adequate density of the markers in case the front expands. On the other hand continuum approaches represent the immersed front on an Eulerian grid as a distribution of some scalar function. Volume of fluid [3], phase field [4, 5] and level set methods [6] are some of the commonly used approaches. These differ in the mathematical functional form used to represent the interface. Level set method provides a convenient means of modeling motion of a sharp interface as well as computing geometrical properties of the front. Mass conservation, which is a commonly encountered challenge with level set approach, can be achieved using high order numerical techniques for definition of the function. In addition to interface tracking, the level set function is also used to formulate a ghost-fluid based method for application of boundary conditions on the immersed front.

4.1 Level Set Method

Level set method uses a signed distance function which is continuous across the interface. The iso-contour corresponding to level set value of zero can be identified as an interface. The level set function, $\varphi(\vec{x})$, is defined as the shortest Euclidean distance from a location $\vec{x}$ to the interface, such that it satisfies

$$|\nabla\varphi| = 1 \ . \tag{10}$$

Dynamic interfaces are modeled by advecting φ in time using appropriate models for the interface propagation speed. Interface is implicitly captured by the zero level set iso-contour at any instant in time. The following equation represents advection using a continuum velocity, $\vec{u} = [u_x \ u_y \ u_z]^{\mathrm{T}}$:

$$\frac{\partial\varphi}{\partial\tau} + \vec{u}\cdot\nabla\varphi = 0 \ . \tag{11}$$

It is more convenient for certain applications [1, 7, 8] to use front normal speed, S, for propagating the interface rather than a continuum velocity. In such problems, the level set function can be advected using Eq. 8. The speed, S, can be a modelled quantity defined in the entire domain [9] such that it converges to the actual front speed as $\varphi \to 0$. It can also be computed on the interface and extended away from it by solving Eq. 7 [8]. Since the level set function, φ, is continuous and defined in a wide region around the interface, computation of interface normals and curvature becomes straightforward through the use of numerical derivative operators [6, 10, 11]. However, maintaining the signed distance property of level set function is challenging. Re-assigning a distance value to the level set function after advection becomes necessary and has remained a central focus of the method in various literature [12]. The treatment, also called reinitialization, is commonly found to alter the instantaneous position of the interface and add/remove unphysical mass from the domain. Mass conservation with classic reinitialization approaches is a major limitation of the level set method for modeling interface motion. A detailed discussion on the reinitialization of level set function is presented below.

Given a level set function, φ, the objective of reinitialization is to derive the distance function, Φ, such that it satisfies $|\nabla\Phi| = 1$. Most level set solvers adopt a pseudo time marching approach pioneered by Sussman *et al.* [6] where Eq. 10 is converted into an ordinary differential equation by adding a pseudo time derivative. The modified equation is solved to steady state with the initial field $\varphi = \varphi_0$. The method introduces deviation in the location of the interface and lacks mass conservation property. On the other hand direct solution algorithms include the fast marching scheme [13]. The method propagates distance information away and downwind from the original interface using first order upwind stencils for the partial spatial derivatives in Eq. 10. Prior knowledge about the upwind direction is necessary which makes parallel implementation difficult. The fast sweeping approach [14, 15, 16] was developed based on the fast marching scheme to enable parallel implementation. High order accuracy in the distance field was also shown with the use of weighted essentially non-oscillatory (WENO) finite differences [17, 18]. The major challenge with fast sweeping method is that it requires distance information at grid points close to the interface which can be taken as boundary conditions while solving Eq. 10. A common technique to populate this information is to obtain high order interpolants [19] to initialize distance values at interface bounding grid points. Such methods require additional computations and an iterative approach, adding to the computational time for reinitialization.

In the current work, a novel approach to populate the boundary conditions for the fast sweeping method has been developed. Prior to applying the fast sweeping algorithm, the interface is anchored in its original position by initializing high order distance functions at grid points immediately next to the interface using information only from the existing state. The fast sweeping method implementation is based on the work of Zhao *et al.* [15] with a different approach for upwinding. Efficient implementation of the fast sweeping method in parallel has already been shown in literature. The anchoring process, as will be shown later, is an algebraic equation and does not require iterations. A combination of anchoring and fast sweeping methods provides excellent scability and makes the implementation massively parallelizable.

Figure 2 shows a schematic of a mesh along with the implicitly defined interface. The objective is to reinitialize a distance function at all of the mesh locations such that the interface position does not change. The mesh locations that are immediately adjacent to the interface are called bounding nodes and are shown as filled symbols in Fig. 2. Since the level set function, φ, is a signed function, the bounding nodes on either side of the interface will have opposite signs for $\varphi - \varphi_0$. Deriving the distance function at the bounding nodes is called anchoring and serves two purposes. Anchoring needs to ensure that the position of the interface is preserved. Anchoring also provides algebraic constraints that are used to solve the distance function at all other points in the domain. These two steps are presented in detail below.

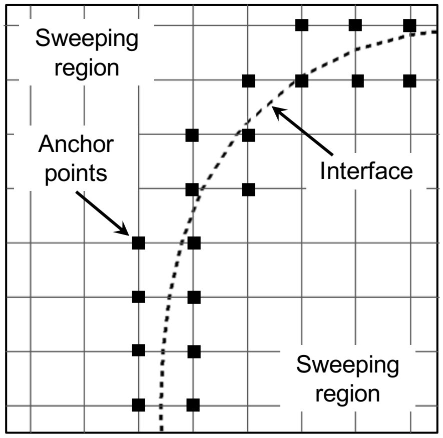

Figure 2. Schematic of the Cartesian mesh showing the location of the interface defined implicitly as $\varphi = \varphi_0$. The mesh locations that are adjacent to the interface are shown as filled symbols. Remaining grid points form the sweeping region.

4.1.1 Anchoring at the bounding nodes

The anchoring step takes the level set function, φ, as input to determine the distances at the bounding nodes. The spatial derivatives of φ are obtainable through finite difference operators. We can also define a local normal, $\hat{n}$, to the iso-contours of φ as $\hat{n} = \nabla\varphi/|\nabla\varphi|$. The normal points towards the direction of increasing φ. Let n denote the signed normal distance along the direction $\hat{n}$. Let the value of the level set function at a bounding node B be φ_B. We expand φ in the neighborhood of B using Taylor's series as,

$$\varphi = \varphi_{\mathrm{B}} + \delta n \frac{\partial \varphi}{\partial n} + \frac{1}{2}\delta n^2 \frac{\partial^2 \varphi}{\partial n^2} + \dots \ . \tag{12}$$

We linearize the equation with respect to δn as,

$$\varphi = \varphi_{\mathrm{B}} + \delta n \frac{\partial \varphi}{\partial n} + \frac{1}{2}\delta n \delta\varphi \left(\frac{\partial \varphi}{\partial n}\right)^{-1} \frac{\partial^2 \varphi}{\partial n^2} + \dots \ . \tag{13}$$

If Φ_{B} is the reinitialized distance function at the point B, then substituting $\varphi = \varphi_0$, $\delta n = -\Phi_{\mathrm{B}}$ and $\delta\varphi = -(\varphi_{\mathrm{B}} - \varphi_0)$ in the above equation will yield a relation for the unknown Φ_{B} in the following form:

$$\varphi_0 = \varphi_{\mathrm{B}} - \Phi_{\mathrm{B}} \frac{\partial \varphi}{\partial n} + \frac{1}{2}\Phi_{\mathrm{B}} \left(\varphi_{\mathrm{B}} - \varphi_0\right) \left(\frac{\partial \varphi}{\partial n}\right)^{-1} \frac{\partial^2 \varphi}{\partial n^2} + \dots \ . \tag{14}$$

Denoting the first and second derivatives of φ in the normal direction $\hat{n}$ as $\partial\varphi/\partial n = \varphi'$ and $\partial^2\varphi/\partial n^2 = \varphi''$, we derive an expression for the distance function at the bounding node B as:

$$\Phi_{\mathrm{B},2} = \left(\frac{\varphi_{\mathrm{B}} - \varphi_0}{\varphi'}\right)\left(1 - \frac{1}{2}\frac{(\varphi_{\mathrm{B}} - \varphi_0)}{\varphi'^2}\varphi''\right)^{-1} \ . \tag{15}$$

The subscript 2 in Eq. 15 denotes that the expression was obtained by including up to the second order derivative terms in the Taylor's series in Eq. 12. It will be shown later in the results section that Eq. 15 yields a third order accurate Φ and a second order accurate $\nabla\Phi$. Also, note that the first term in Eq. 15 corresponds to a first order anchoring [20] for the distance function at B. That is,

$$\Phi_{\mathrm{B},2} = \Phi_{\mathrm{B},1}\left(1 - \frac{1}{2}\frac{(\varphi_{\mathrm{B}} - \varphi_0)}{\varphi'^2}\varphi''\right)^{-1} \ , \tag{16}$$

where

$$\Phi_{\mathrm{B},1} = \frac{\varphi_{\mathrm{B}} - \varphi_0}{\varphi'} \ . \tag{17}$$

The anchoring step needs the first and second derivatives of the level set function φ normal to the surface, which are obtained from the derivatives in the Cartesian directions, x, y and z as

$$\frac{\partial \varphi}{\partial n} = |\nabla\varphi| \ , \tag{18}$$

$$\frac{\partial^2 \varphi}{\partial n^2} = \nabla\varphi^{\mathrm{T}} H(\varphi) \nabla\varphi \tag{19}$$

where, $H(\varphi)$ is the Hessian matrix defined as

$$H(\varphi) \equiv \begin{bmatrix} \frac{\partial^2\varphi}{\partial x^2} & \frac{\partial^2\varphi}{\partial x\partial y} & \frac{\partial^2\varphi}{\partial x\partial z} \\ \frac{\partial^2\varphi}{\partial y\partial x} & \frac{\partial^2\varphi}{\partial y^2} & \frac{\partial^2\varphi}{\partial y\partial z} \\ \frac{\partial^2\varphi}{\partial z\partial x} & \frac{\partial^2\varphi}{\partial z\partial y} & \frac{\partial^2\varphi}{\partial z^2} \end{bmatrix} . \tag{20}$$

The second and cross-derivative terms in the Hessian matrix are evaluated using second order central differences.

In the numerical tests that follow, the spatial derivatives needed to calculate $|\nabla\varphi|$ are computed using essentially non-oscillatory (ENO) stencils [18]. Although level set is continuous across the interface, ENO derivatives are needed for stability in case a discontinuity exists within the finite difference stencil in regions of high curvatures. ENO schemes use an adaptive stencil switching between a central difference or upwind scheme such that grid points across a discontinuity are ignored.

4.1.2 Solving at the interior nodes

Once the interface is anchored, the distance function is calculated at the interior mesh points farther away from the interface and beyond the bounding nodes. The distance function values at the bounding nodes provide the boundary condition to solve Eq. 10. We present the first order upwind finite difference formulation for Φ and then extend it to implement higher order derivative operators. The gradient of distance function is written using first order one-sided finite difference operators. The choice of direction for one-sided differencing is determined by the upwinding principle that the information propagate from smaller distance to larger [13]. The distance function at the neighboring point in the x direction, $\varphi_{\mathrm{nb,x}}$, that is chosen for computing the first order one-sided derivative is obtained using,

$$\Phi_{\mathrm{nb,x}} = \begin{cases} \min\left(\Phi_I, \Phi_L, \Phi_R\right) & \text{if } \Phi_I \geq 0 \\ \max\left(\Phi_I, \Phi_L, \Phi_R\right) & \text{if } \Phi_I < 0 \end{cases} , \tag{21}$$

where φ_{L} and φ_{R} are the distance functions at the grid points adjacent to an interior node, I, on the left and right sides, respectively. The distance function at neighboring mesh points in y and z directions, $\varphi_{\mathrm{nb,y}}$ and $\varphi_{\mathrm{nb,z}}$ can be computed similarly. Eq. 10 is then written in terms of the first order derivatives as

$$\left(\frac{\Phi_{\mathrm{I}} - \Phi_{\mathrm{nb,x}}}{h}\right)^2 + \left(\frac{\Phi_{\mathrm{I}} - \Phi_{\mathrm{nb,y}}}{h}\right)^2 + \left(\frac{\Phi_{\mathrm{I}} - \Phi_{\mathrm{nb,z}}}{h}\right)^2 = 1 , \tag{22}$$

where h denotes the mesh spacing which is assumed to be uniform in the three directions. However, it is straight forward to rewrite Eq. 22 when the mesh spacing is different in the three directions. An iterative solution of Eq. 22 is the first order accurate fast sweeping method presented in Ref. [14, 16].

We extend this method to allow a higher order accurate solution by first modifying Eq. 21 as,

$$\Phi_{\mathrm{nb,x}} = \begin{cases} \min\left(\Phi_{\mathrm{I}}, \Phi_{\mathrm{I}} - h\left(\frac{\partial\Phi}{\partial x}\right)^-_{\mathrm{I}}, \Phi_{\mathrm{I}} + h\left(\frac{\partial\Phi}{\partial x}\right)^+_{\mathrm{I}}\right) & \text{if } \Phi_{\mathrm{I}} \geq 0 \\ \max\left(\Phi_{\mathrm{I}}, \Phi_{\mathrm{I}} - h\left(\frac{\partial\Phi}{\partial x}\right)^-_{\mathrm{I}}, \Phi_{\mathrm{I}} + h\left(\frac{\partial\Phi}{\partial x}\right)^+_{\mathrm{I}}\right) & \text{if } \Phi_{\mathrm{I}} < 0 \end{cases} , \tag{23}$$

which is identical to Eq. 21 if two point left and right stencils are used to arrive at the spatial derivatives $(\partial\Phi/\partial x)^-$ and $(\partial\Phi/\partial x)^+$. We obtain a higher order accurate solution for Φ_{I} by using a wider stencil and higher order upwind operators for $\partial\Phi/\partial x$ in Eq. 23 and then solving Eq. 22. This is repeated iteratively until Φ_I has converged. Zhang *et al.* [17] propose high order WENO operators for these derivatives. However, it has to be noted that the WENO stencils are not strictly one-sided and do not follow monotonic convergence when the anchoring is performed through reinitialization, and without using analytical distances at the bounding nodes. Since we are computing the derivatives using one sided stencils, we can obtain monotonic convergence and stable reinitializations as will be demonstrated using canonical test problems.

A schematic of the standard three point stencil is shown in Fig. 3. Stencils 'A' and 'B' are both monotonically converging. The difference between the two stencils is that 'B' contains grid points which belong to the other side of the interface with respect to the grid point being solved for. However, once anchored, the value of Φ at bounding points (shown by solid rectangles) is a signed distance function which is monotonic. There are exceptions to the monotonic convergence when iterating for Φ_I using Eq. 22 as shown by the two triangles within stencil 'C' in Fig. 3. A second order upwind stencil is three point wide, due to which the solutions at the two mesh points indicated by the triangles are coupled with one another. This occurs when the distance function is not monotonic within the stencil. In such situations, the convergence of the solution can be weak or unstable. To overcome this difficulty, we use an under-relaxation of the iterative solution whenever the stencil has a non monotonic variation of the solution.

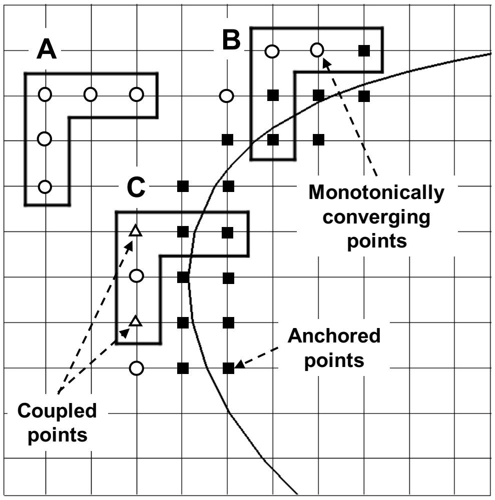

Figure 3. Schematic of three point upwind finite difference stencils for fast sweeping method.

4.2 Immersed Boundary Method

Discretization of derivatives in space near an interface needs to be carefully formulated to apply immersed boundary condition and ensure stability of the numerical scheme. To address this problem an implementation based on ghost fluid method [21, 22] using level set information is outlined below. Finite difference stencil near an immersed interface may involve grid points across the surface where physically correct values of the variables and material properties might not exist. An example of such a situation is shown in Fig. 4. The highlighted stencil represents central difference scheme at a grid point in the domain given by $\varphi > 0$ adjacent to the front. In the context of the current application, this domain represents the gas phase. The stencil involves grid points belonging to the solid phase, $\varphi < 0$. Variables such as temperature field and concentration as well as material properties may exhibit a jump across the sharp front given by $\varphi = 0$. A robust formulation is developed which ensures stability of the numerical scheme. The grid points across an interface are treated as ghost points and populated by considering information available on the immmersed interface such as a boundary condition. Figure 5 outlines the steps involved in the formulation assuming either Dirichlet or Neumann condition is applied at the surface. An extension of the method to apply a reactive boundary condition will be described later.

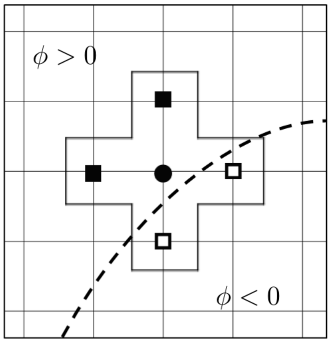

Figure 4. A standard second order central difference stencil at a grid point (solid circle) near an immersed interface. Certain neighboring points belong to opposite domain (open squares) where physical values are not available.

The first step is to project the function values at grid points onto the interface using flux information (Neumann condition) or compute normal gradient using the function value on the front (Dirichlet condition). As shown in Fig. 5 the grid points adjacent to the interface are denoted by i and the projection points are i'. The corresponding level set values at the grid points are φ_i, which are also the distances ii'. Let C be the reactive scalar. The following equation shows a first order accurate projection step for Dirichlet and Neumann boundary conditions on the interface:

$$\left(\frac{\partial C}{\partial n}\right)_{i'} = \frac{C_i - f(i')}{\varphi_i} \quad \text{(Dirichlet)} \tag{24a}$$

$$C_{i'} = C_i - g(i')\varphi_i \quad \text{(Neumann)} \ , \tag{24b}$$

where $C^I = f$ and $(\partial C/\partial n)^I = g$ denote the Dirichlet and Neumann conditions to be applied on the front. Once the projection values are determined, these values are interpolated at the projection point G' using

$$\left(\frac{\partial C}{\partial n}\right)_{G'} = \frac{\Sigma w_{i'} \left(\frac{\partial C}{\partial n}\right)_{i'}}{\Sigma w_{i'}} \quad \text{(Dirichlet)} \tag{25a}$$

$$C_{G'} = \frac{\Sigma w_{i'} C_{i'}}{\Sigma w_{i'}} \quad \text{(Neumann)} \ . \tag{25b}$$

The weights, w, depend only on the geometry of the interface and are chosen such that it is maximum for projection points closest to G'. The final step is to project function value to ghost point G using the

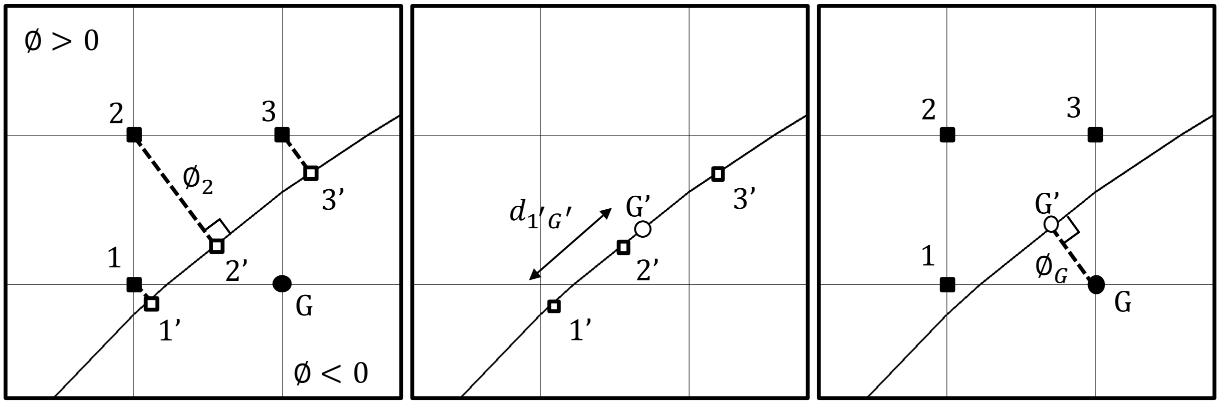

(a) Projection: Grid to interface **(b) Interpolation** **(c) Projection: Interface to grid**

Figure 5. Immersed boundary formulation using level set information. The three major operations: (a) projection from grid to interface, (b) interpolation along the interface and (c) projection from interface to grid are shown. Solid and empty markers denote grid points and projection points respectively. Square and circular markers represent real and ghost domains respectively.

interpolated gradient or the value as

$$C_G = f(G') + \left(\frac{\partial C}{\partial n}\right)_{G'} \varphi_G \quad \text{(Dirichlet)} \tag{26a}$$

$$C_G = C_{G'} + g(G')\varphi_G \quad \text{(Neumann)}\ . \tag{26b}$$

At the end of these steps, the function values at ghost point G is such that the specified boundary condition is satisfied on the front, and standard finite difference operators can be applied at real grid points bounding the interface.

The method can be extended to apply a reactive boundary condition given by Eq. 5. We briefly outline the scheme using explicit formulation, suitable for iterative solution of Poisson equation. The normal gradient of C on the surface can be given by

$$\left(\frac{\partial C}{\partial n}\right)_{G'} = r(C|_{G'})\ . \tag{27}$$

The value of $C|_{G'}$ is computed using Eqs. 24b and 25b with $g(G') = r(C|_{G'})$ evaluated explicitly. Using Eq. 27, the normal gradient is updated and the ghost point is populated with C_G computed from Eq. 26b. The non-linear boundary condition is coupled with a Poisson solver described in the following section. At every iteration, the normal gradient is updated based on the existing distribution of the scalar in the vicinity of the interface, which is subsequently utilized to populate the ghost zone.

4.3 Diffusion Solver

The reactive scalar transport is governed by a Poisson equation with a non-linear boundary condition on the immersed solid surface (Eqs. 5 and 6). The Laplacian operator, ∇^2 is discretized in space using second order central difference formula. A Jacobi method using underrelaxation is implemented to solve the discretized Poisson equation iteratively. The scheme is outlined in Ref. [23] and its detailed implementation can be found in Ref. [24]. The immersed boundary method described in Section 4.2 is used to apply the non-linear reactive boundary condition on the immersed surface given by the zero level set contour. The ghost points are updated at each iteration explicitly. As the method is explicit, parallelization is straightforward.

4.4 Level Set Initialization

Importing complex geometries to represent embedded surfaces into a structured mesh code is a commonly encountered challenge, specifically in cases where the initial geometry comes from experimental data through imaging methods, or if the geometry is too complex to represent using analytical functions of spatial coordinates. For industrial relevance, these geometries are typically constructed using solid modeling tools where surfaces are discretized. To enable utilizing such geometries without making any simplification, a utility developed in Quilt transforms a triangulated surface into an implicit representation on a structured mesh using the level set technique. The level set function is formed such that its zero contour aligns with the surface being imported. The algorithm used in Quilt is described here for the case where the initial triangulated geometry provides the location of vertices and the normal vector of each triangle. Normal vector is only used to distinguish the two phases separated by the surface.

The basic element of the formulation is to compute the shortest distance of a point in space from a triangle. The point represents any grid point of the structured mesh and the triangle represents any element of the surface. There are three possibilities for a point on the triangle to be closest to the grid point: (1) it could be the projection of grid point on the triangle, (2) projection of grid point on one of the sides of the triangle, or (3) one of the vertices of the triangle. The three possibilities are shown in Fig. 6 follwing which, the algorithm is explained.

Let us denote the point under consideration (grid point of a structured mesh) as P. The objective is to locate a point X belonging to a particular triangle such that the distance PX is minimum. We start by locating the projection of P on the plane formed by the triangle, called Q. There are two possibilities for the location of Q:

1. Q falls within the triangle, it is the closest point to P. This possibility is shown by case 1 in Fig. 6.
2. Q falls outside the triangle, the point closest to P could be one of the following:
    (a) A projection of P onto one of the sides of the triangle (case 2 in Fig. 6).
    (b) One of the vertices of the triangle (case 3 in Fig. 6).

    In this case, the projections, R, of P on all of the sides are obtained. If R does not belong to the triangle, it is omitted from further calculations. The shortest distance of P from the triangle is then computed as the minimum of all PR and PV, where V denotes the vertices of the triangle. The corresponding point will be closest to P.

The level set function at the grid point is defined as $\pm d$ where d is the shortest distance computed above. The sign is determined from the direction of normal vector of the particular triangle. The process is repeated for all triangles belonging to the geometry and a level set value is determined as being one that has the smallest magnitude. The pseudo code shown below outlines the process of finding the shortest distance,

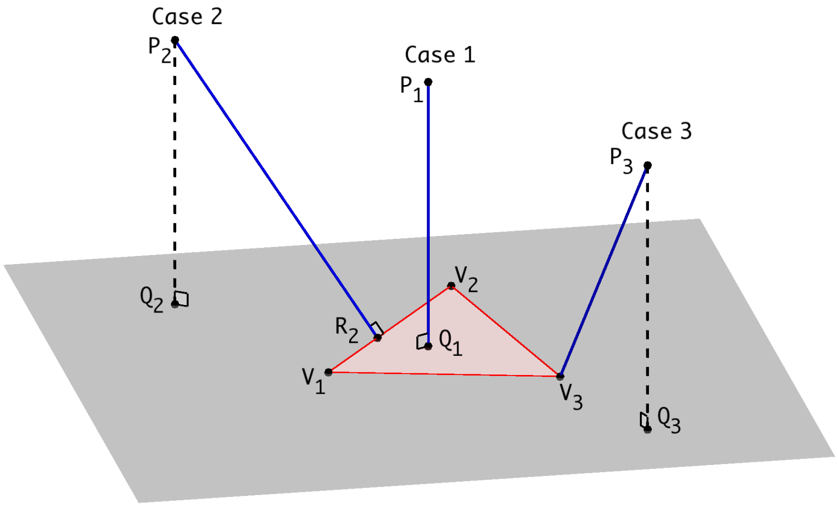

Figure 6. Example configuration showing possibilities for the shortest distance of a point (P_1, P_2 and P_3) from a triangulated surface. Projection of P_1 falls within the triangle while those of P_2 and P_3 (dotted) do not. The minimum distances (solid) may be formed with projection to the plane of triangle (P_1Q_1), projection to side of the triangle (P_2R_2) or with one of the vertices (P_3V_3).

d from a set of triangles. The computational implementation uses a library, Eigen3, for performing the vector algebra used for determining the projections and intersection points.

```
SET d = large
FOR each triangle in geometry DO
  SET d1 = large
  Q = projection of P on triangle
  IF Q within triangle THEN
    d1 = PQ
  ELSE
    d1 = MIN(PV1,PV2,PV3)
    FOR each side of triangle DO
      R = projection of P on side
      IF R within side THEN
        d1 = MIN(d1,PR)
  d=MIN(d,d1)
```

An example of the transformation is shown below. The geometry represents a plain weave having one pair of tows (warp and weft). The triangulated geometry in Fig. 7 (a) is used as the input for the transformation and the resultant signed distance function is shown in Fig. 7 (b) along with a shaded contour representing the zero level set. When the size of the Stereolithography (STL) data (number of triangles) is small each grid point can sweep through all triangles and find the minimum distance. However, if the initial geometry is too large, as in the case of fiber resolved 5hs weave, the cost of initialization increases quickly with the total number of surface elements. An efficient initialization procedure is sought in such cases and has been explained below.

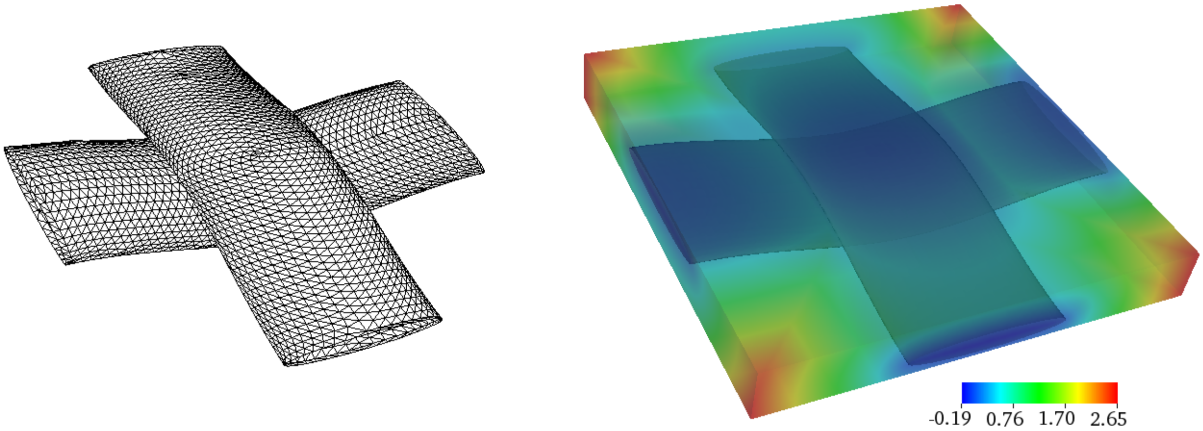

(a) Triangulated surface **(b) Level set function on structured mesh**

Figure 7. Transformation of a triangulated plain weave (a) to a level set function on a structured mesh (b). The color shows distance function while shaded contour shows the zero level set representing the surface.

4.5 Preform Geometry Assembly

Initializing the level set function on a structured mesh for a fiber resolved weave is challenging owing to the large number of triangles required to discretize the surface as well as the number of grid points in the structured mesh. Therefore, an alternative approach was needed to initialize the level set function. The process involves two basic steps: geometric distance calculation at grid points close to the surface, and fast sweeping solution of the Eikonal equation at farther points. The transformation is similar to the reinitialization method described in Section 4.1 with the geometric distance computation providing the algebraic constraint for the fast sweeping method. Moreover, the number of triangles to be swept in the geometric process is also limited to a small neighborhood.

The present work involved initialization of level set function representing a fiber resolved 5hs weave preform on a structured mesh. The triangulated geometry is shown in Fig. 8. The preform comprises of five stacked layers of a 5hs elementary weave, each having a random offset (Fig. 9). Each weave has five pairs of warps and wefts shown in Fig. 10. It is clear that a warp and a weft are geometrically related through a series of simple rotational transformations: 90° about its normal and 180° about its axial direction. Each warp/weft in a layer can be obtained by translation along its axial direction as shown in Fig. 11. Additional upstream triangles required for translation can be easily populated using periodicity. Thus, it can be understood that all the elements involved in the construction of the layered 5hs preform can be obtained from a single warp or a weft through geometric transformations applied to the set of triangles in the discretized surface.

The structured mesh domain for the preform can be divided into smaller domains, each representing a warp or a weft. The geometric transformation needs to be applied on each of the elementary domains independently, allowing parallel implementation and requiring significantly less memory. Moreover,

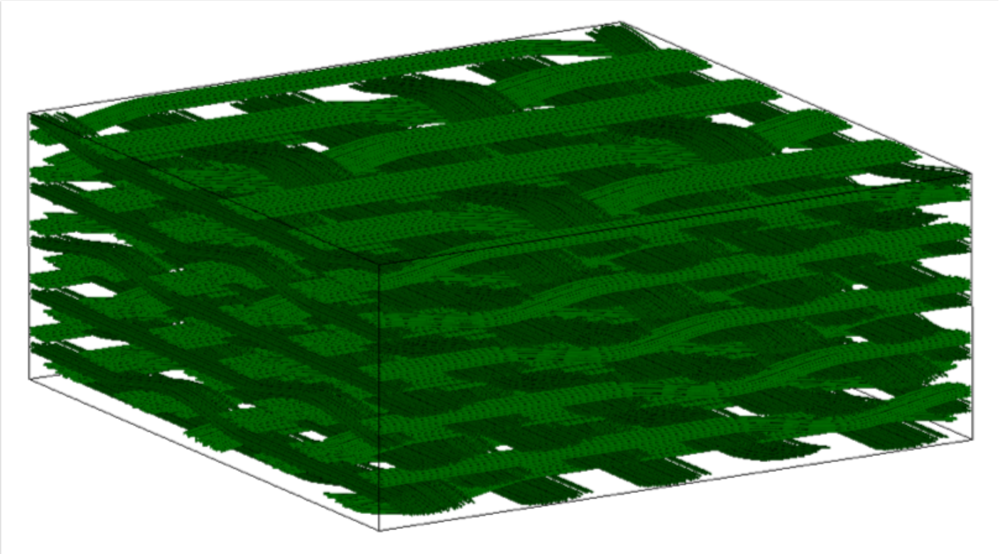

Figure 8. Fiber resolved geometry of a 5 layered 5hs weave. Each of the warp and weft comprises of a collection of approximately 50 fibers. The geometry is composed by assembling together various elements created from a single fiber bundle using a series of geometric transformations on the triangulated surface and converting it to a level set representation on a structured mesh. Structured mesh comprises of 10B grid points, required to resolve each individual fiber.

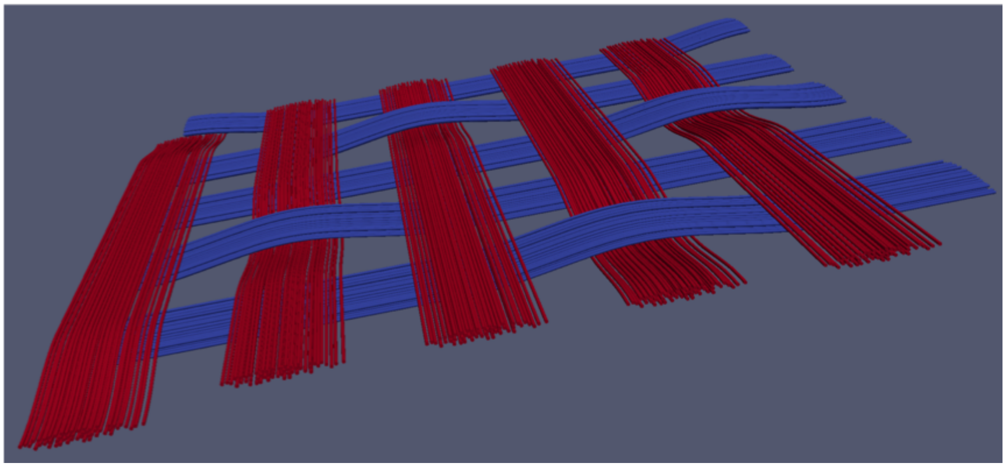

Figure 9. Single layer of a 5hs weave consisting of five warp-weft pairs.

distance computation at this stage is only performed at grid points close to the surface. The rest of the points are initialized with ∞. The number of triangles swept by each grid point is limited within a small neighborhood to conserve computational time. Once the level set function is initialized locally, the structured mesh blocks can be assembled into a larger domain representing the complete preform. The assembly involves defining the global level set function, φ_g, in terms of the local values, φ_l, as

$$\varphi_g = \min(\varphi_g, \varphi_l) \ , \tag{28}$$

where l represents each of the structured blocks and g represents the domain of the preform. Following the

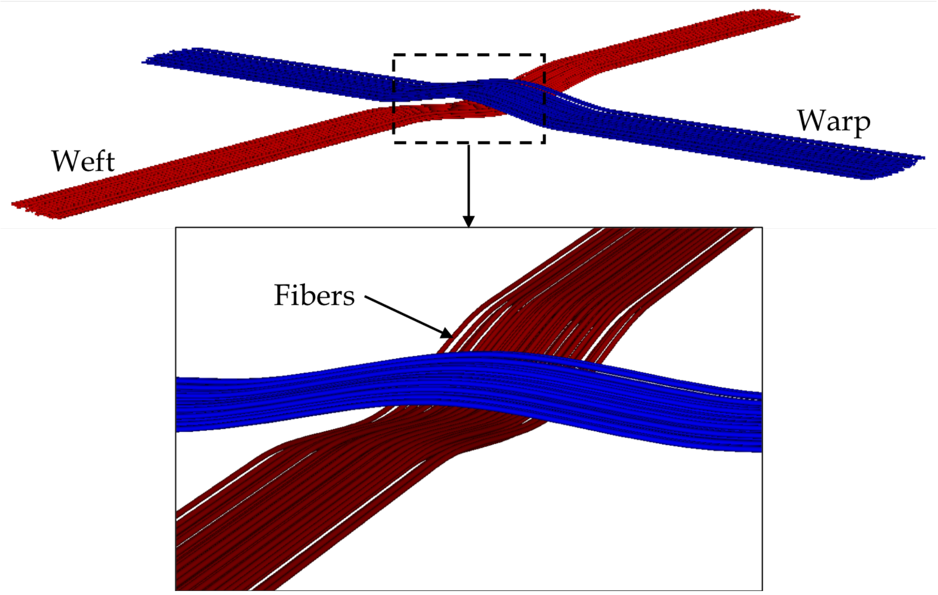

Figure 10. A warp-weft pair in a 5hs weave, each consisting of 50 fibers. The bundles are geometrically related through simple coordinate transformations.

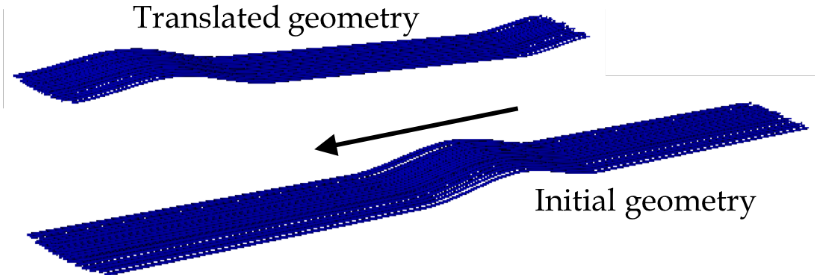

Figure 11. Translation of triangles in a bundle of fibers. Each warp or weft in a single layer can be obtained through translation by specific offset.

initialization, the level set solver applies a fast sweeping algorithm to obtain distance function in the entire domain by solving the Eikonal equation. The flow chart in Fig. 12 shows the complete process of generating a layered preform geometry through level set initialization from a single bundle of triangulated fibers (warp). The first two stages (from the top) involve simple coordinate transformations of the triangles. The third stage represents the geometric distance initialization. The last two stages assemble the structured blocks into layers and subsequently, the preform. The assembled function becomes an input to the level set solver.

4.6 Code Description

Quilt is a high order finite difference Direct Numerical Simulation (DNS) software for reacting multiphase flows through porous media. The code has been developed specifically for high fidelity simulations of reacting interfacial flows at conditions encountered in chemical and material synthesis applications. It

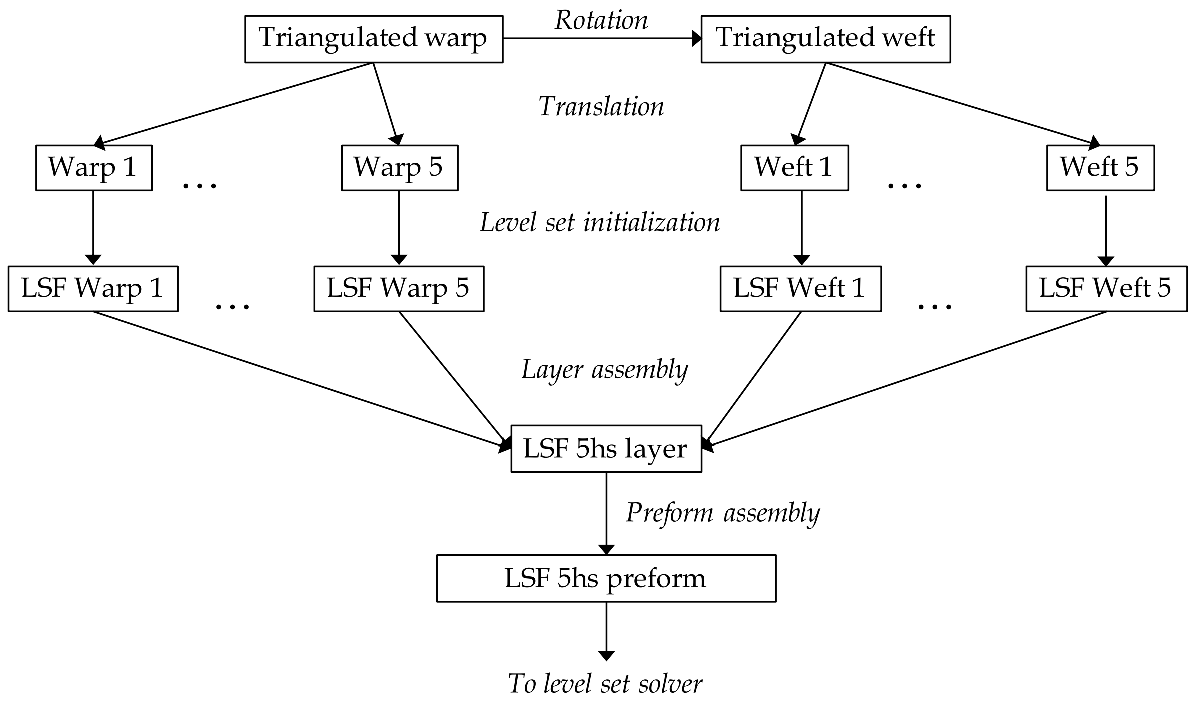
Triangulated warp
Rotation
Triangulated weft
Translation
Warp 1
…
Warp 5
Weft 1
…
Weft 5
Level set initialization
LSF Warp 1
…
LSF Warp 5
LSF Weft 1
…
LSF Weft 5
Layer assembly
LSF 5hs layer
Preform assembly
LSF 5hs preform
To level set solver

Figure 12. Methodology to initialize level set function (LSF) on a structured mesh for a fiber resolved layered 5hs preform from a single triangulated fiber bundle.

solves the variable density, incompressible flow equations with algorithms that are geared towards the low speed flow regimes, typically encountered in materials processing and manufacturing applications. In addition, Quilt also includes interface tracking capability for capturing sharp multi-material fronts. It has been written in modern C++ and has a distributed memory parallel model based on structured mesh domain decomposition. Quilt uses the Kokkos performance portable library for abstractions of the data layout, memory and execution spaces and has been ported to multi-core and Graphics Processing Unit (GPU) accelerated systems.

5. RESULTS AND DISCUSSION

Simulations are performed for a specified non-dimensional Thiele modulus,

$$K \equiv \frac{\tau_{\mathrm{diff}}}{\tau_{\mathrm{chem}}} \ . \tag{29}$$

Eq. 4 gives the Thiele modulus in terms of the physical parameters used in the present DNS simulations. The Thiele modulus represents the CVI processing operating condition (the fixed pressure and isothermal temperature determining the chemical kinetic rate and reagent diffusivities).

Figure 13 shows partially-densified weaves from the simulations choosing a constant Thiele modulus of (b) $K = 0.001$ and (c) $K = 0.1$. The ultimate porosity has been reached in both cases. In Fig. 13a, the initial unit-cell five-harness satin woven preform that was used in both simulations is shown. Fresh reactants diffuse into the preform from both the top and bottom, the vertical or through-thickness direction.

At $K = 0.001$, $\tau_{\text{diff}} << \tau_{\text{chem}}$ and the ultimate porosity is low due to the relatively fast diffusive timescale as compared to the slow chemistry timescale. While at $K = 0.1$, the chemistry is sufficiently fast as compared to diffusive transport and the ultimate porosity is relatively high due to the pore closures at the outer plys. The pore closures are observed in Figs. 14 and 15 for the $K = 0.001$ and $K = 0.1$ cases, respectively.

The robustness and generality of the level-set approach to multiphase modeling allows the CVI densification simulations to be performed for any arbitrary geometry, including geometries at higher levels of detail than that shown in Figs. 13–15. For example, Fig. 16 shows the porosity field for the fiber-resolved preform of Fig. 13. The simulation data can therefore be used to understand residual porosity (manufacturing quality) trends for different preform geometries (*e.g.*, ply layup strategies), as well as trends in each of their densification times (manufacturing times) as a function of the preforming strategy.

The resulting high-fidelity DNS data can also serve to develop mean-field closure models required to perform more practical furnace-scale Computational Fluid Dynamics (CFD) simulations. In furnace-scale CFD simulations, the detailed spatial gradients shown in Figs. 13–16 are represented by only a single computational cell, *i.e.*, single averaged values. This is required such that the larger-scale details of the CVI furnace geometry can be resolved while maintaining practical computational solution times.

In the remainder of this report, two illustrative examples are given for the practical application of the DNS data. The DNS data is used to develop porous media modeling for the physical phenomena that is required in the mean-field, furnace-scale CFD simulations. This includes modeling the dependence of the unresolved surface-to-volume ratio on the porosity (one of fundamental “structure functions” of the unresolved CVI densification fronts) and the scaling of the diffusivity and permeability to the structure functions.

5.1 Modeling of the structure functions

The fiber-weave specific structure functions includes one or more effective length scales and the surface-to-volume ratio of the porous media. The porous media geometry is resolved by the DNS, but not by the mean-field (modeled) CFD simulation.

The structure functions rely on an assumed quasi-steady relationship to the porosity at the unresolved scale, *e.g.*,

$$\sigma = f(\phi, D) \ , \tag{30}$$

where σ (m^{-1}) is the unresolved surface-to-volume ratio, ϕ is the void volume fraction or porosity, and D is an effective diameter.

In the modeled CFD simulations, the local porosity is known from the concurrent solution of

$$\frac{d}{dt}\phi = -\sigma k y \ , \tag{31}$$

given here for present simplified, one-step deposition chemistry case.

The structural modeling challenge stems from the unresolved evolving deposition fronts which lead to deviations from the simple structural evolution of non-interacting tows or fibers. In the idealized case

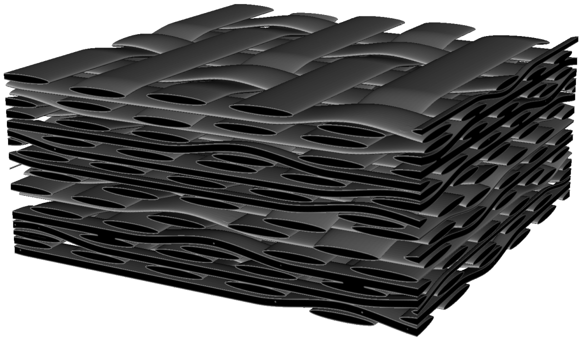

(a) Preformed geometry

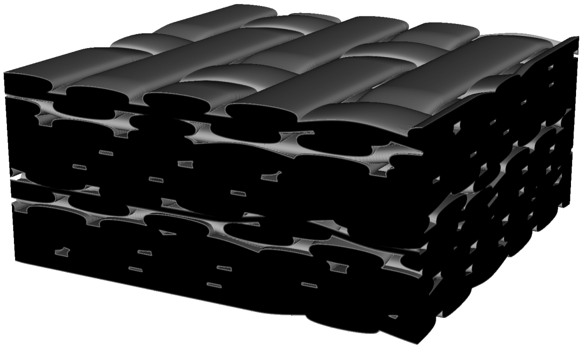

(b) Densified weave at $K = 0.001$

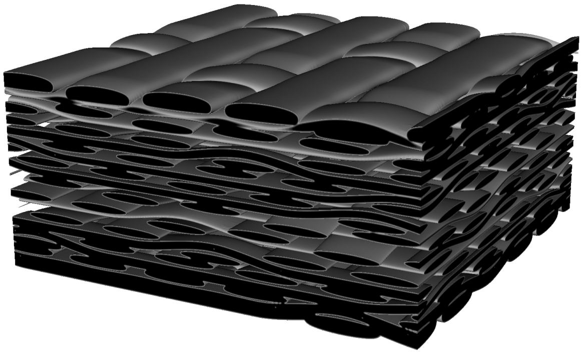

(c) Densified weave at $K = 0.1$

Figure 13. Partially-densified woven preforms from the DNS simulations. The original weave prior to CVI processing is shown in (a). Figures (b) and (c) show the densified weave after processing. In (b), the Thiele modulus is $\boldsymbol{K = 1 \times 10^{-3}}$ and the chemical time scale is much larger than transport of vapor. In (c), $\boldsymbol{K = 1 \times 10^{-1}}$ and the chemical timescale is relatively much smaller.

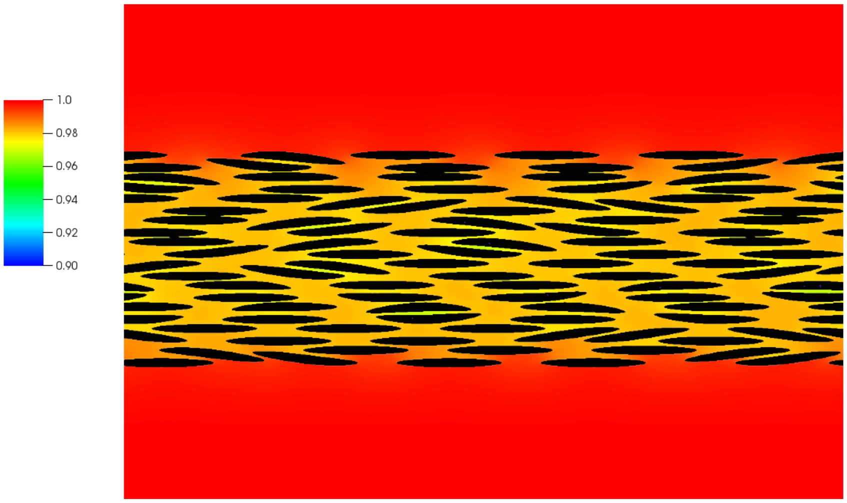

(a) Initial

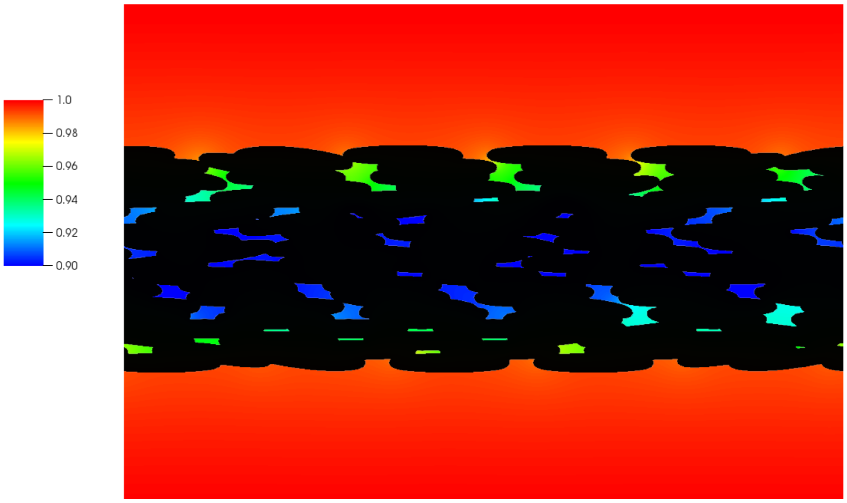

(b) Processed

Figure 14. Cross-section of (a) the initial and (b) processed weave for the $K = 1 \times 10^{-3}$ case shown in Fig. 13. Also shown is the scalar transported through the porous matrix as pseudocolor in the rainbow color scale.

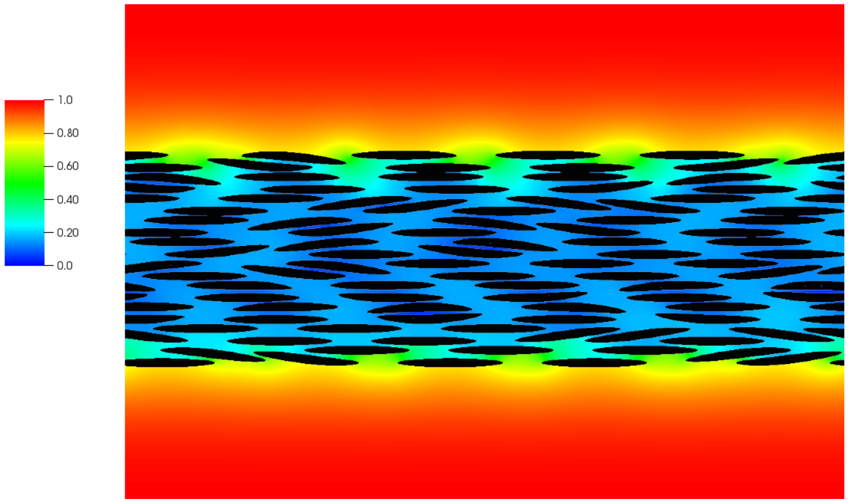
1.0
0.80
0.60
0.40
0.20
0.0

(a) Initial

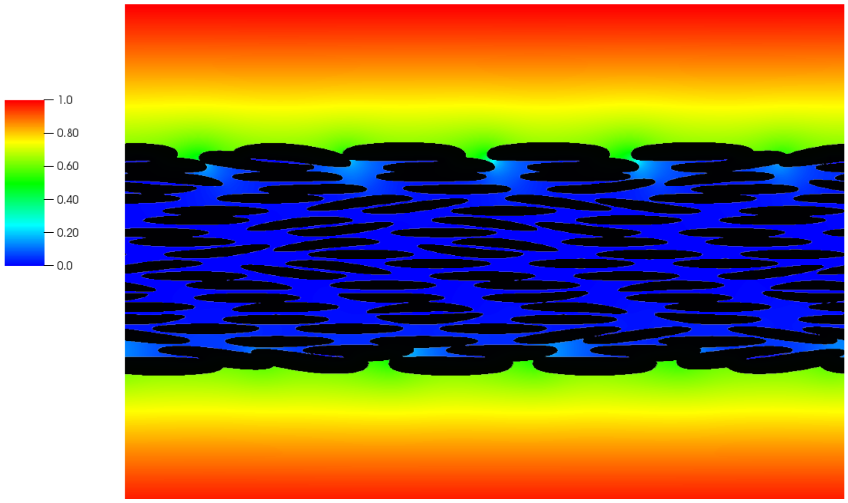
1.0
0.80
0.60
0.40
0.20
0.0

(b) Processed

Figure 15. Cross-section of (a) the initial and (b) processed weave for the $K = 1 \times 10^{-1}$ case shown in Fig. 13. Also shown is the scalar transported through the porous matrix as pseudocolor in the rainbow color scale.

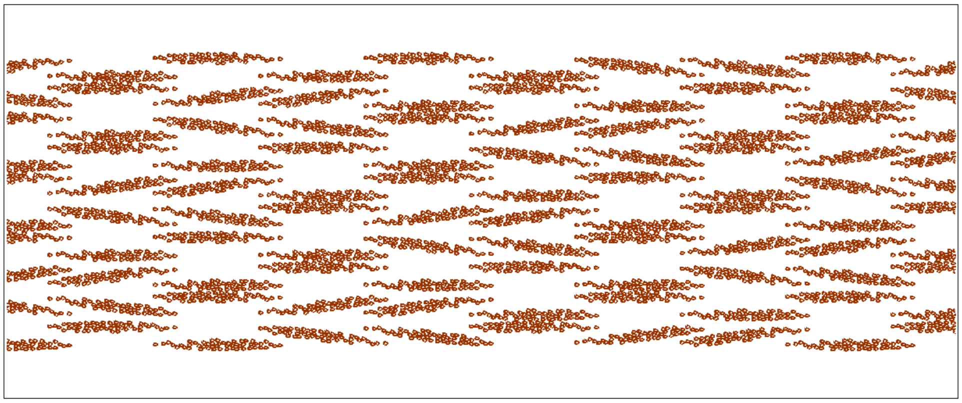

(a) Initial

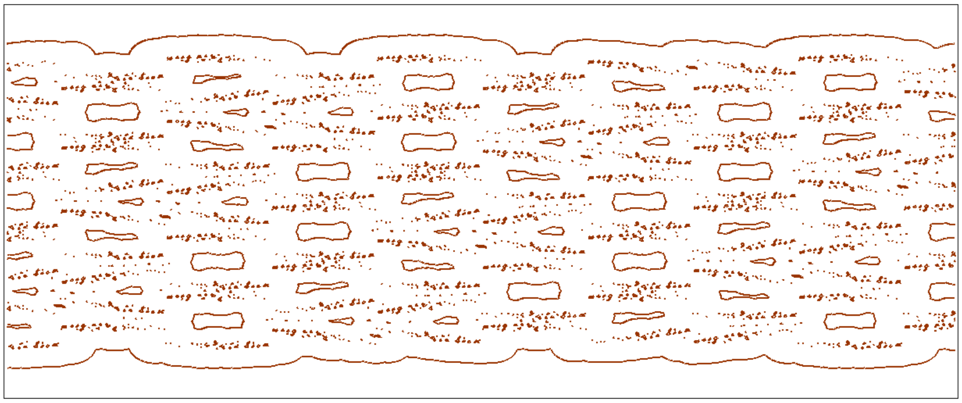

(b) Densified

Figure 16. Illustration of DNS simulations for a fiber-resolved case. Cross-section of (a) the initial and (b) densified weave with the initial preformed geometry composed of tows formed from bundles of 50 fibers each.

where the diameter of each fiber grows uniformly (but not necessarily at a constant rate), the exact quasi-steady relations can be shown to be:

$$\frac{D}{D_0} = \sqrt{\frac{1-\phi_0}{1-\phi}} \quad \text{and} \quad \frac{\sigma}{\sigma_0} = \left(\frac{1-\phi}{1-\phi_0}\right)^{3/2} \quad , \tag{32}$$

where D_0, ϕ_0, and σ_0 are the initial values for the effective diameter, porosity, and surface-to-volume ratio, respectively.

The deviation from structure functions (Eq. 32) can occur at early times as fiber-weave preforms can be composed of non-homogeneously distributed (touching) fibers. Further, the densification can lead to isolated pores, locally inaccessible to precursor infiltration, and therefore increasing the final porosity to a non-zero threshold value, as most notably illustrated by the DNS case above with Thiele modulus $K = 0.1$.

Existing structural models may be classified into two broad categories. Ideally, the goal of both approaches is to derive an analytic formulation like Eq. 32, whose accuracy is known for a particular condition (*e.g.*, Thiele modulus).

1. **Flow-centric modeling approach.** In this approach, the nature of the flow takes modeling precedence, acknowledging a simplified or surrogate representation of the actual woven fiber geometry. Examples here include the node bond model of Starr [25], a flow network model using random overlapping, finite-length capillary tubes by Ofori & Sotirchos [26], and others [27, 28].

   In some of these approaches, the ultimate porosity is treated *ad hoc* invoking a change of variables following [29]:

   $$\phi_a = \alpha(\phi - \phi_p)^\beta \quad ,$$

   where ϕ_a is the "accessible" porosity, ϕ_p is the specified percolation (threshold) value, $\beta = (\phi_0 - \phi_p)/\phi_0$, and $\alpha = \phi_0/(\phi_0 - \phi_p)^\beta$.

   The defining characteristic in this approach is that any finite Thiele modulus effects are assumed to be implicitly accounted for by the semi-empirical correlations themselves. The models are advantageous in that they are readily incorporated into an existing 3-D CFD model of CVI.

   As a representative example in this category, Ofori & Sotirchos [26] give

   $$\sigma = \frac{4}{D_0}\sqrt{-\log(1-\phi_0)}(1-\phi)\sqrt{-\log(1-\phi)} \quad . \tag{33}$$

   This relation does not satisfy the actual initial surface area of woven cloth preforms (*e.g.*, non-overlapping tow or fiber geometries).

2. **Explicit fiber geometry models.** This approach generally invokes the slow chemistry approximation ($K << 1$), but maintains a closer or exact representation of the fiber weave geometry. Examples here include the analytical model of Sheldon & Besmann [30] which approximates a tow with non-overlapping fibers. Guan *et al.* [31, 32] have extended this approach to account for exact geometries using level-sets, but invoke a steady-state assumption for the reagent.

The model of Sheldon & Besmann [30] is used as a representative example here:

$$\begin{aligned}
\frac{D}{D_0} &= \sqrt{1-\left(\frac{\phi_0}{1-\phi_0}\right)\log\left(\frac{\phi}{\phi_0}\right)} && \text{(34a)}\\
\frac{\sigma}{\sigma_0} &= \frac{\phi}{\phi_0}\frac{D}{D_0} && \text{(34b)}\\
\frac{\phi}{\phi_0} &= \exp\left[-\left(\frac{1-\phi_0}{\phi_0}\right)\left(\frac{D^2}{D_0^2}-1\right)\right] \;. && \text{(34c)}
\end{aligned}$$

This relation is not valid for non-homogeneously distributed fibers which are characterized by at least two characteristic geometric length scales (characteristic of tows made of bundled fibers).

Figure 17 compares the surface-to-volume models in Eqs. 33 and 34 to the DNS data. Symbols show the nondimensional surface-to-volume ratio (σ/σ_0) against the normalized porosity (ϕ/ϕ_0) at regular time intervals computed from the DNS simulations. Black circles represent the "Baseline" preform geometry, where the $N = 10$ individual woven plys have been randomly stacked in the through-thickness or vertical direction (*cf.* Figs. 13–15). Figure 17 shows that a lower ultimate porosity is reached at the lower Thiele modulus, as physically described in the discussion surrounding Figs. 13–15. Lines in Fig. 17 are the analytical functions: Eq. 33 is given by the magenta dash-dot lines, Eq. 34 by the dash-dash lines. Equation 33 predicts that σ/σ_0 exceeds unity, while Eq. 34 shows that σ/σ_0 always decreases with porosity for all the preform geometries considered here.

DNS results from two other preform geometries are shown in Fig. 17. In the Overlap preformed geometry (blue squares), each ply is offest from its adjacent ply. In this configuration, all even and odd numbered plys are vertically aligned. The fixed offset yields the largest tortuosity through the weave. In the Aligned configuration, all plys are vertically aligned and therefore this preform geometry is characterized by the lowest tortuosity. In all three configurations, all individual plys are identical, the total number of plys are the same, and the total preform volume is the same.

The analytical models Eq. 33 and Eq. 34 are independent of Thiele modulus. Focusing first on results from the Baseline preform (black circles) of Fig. 17, a clear Thiele modulus dependence is observed. At relatively high Thiele modulus ($K = 0.1$), the surface area initially increases, then decreases just before the ultimate porosity is reached. This trend is captured by Eq. 33, although some discrepancy arguably exists in the exact magnitudes. At low Thiele modulus ($K = 0.001$), the surface area of the Baseline preform monotonically decreases for all CVI densification times. In this limit, both trends and magnitudes are not described well by Eq. 33, while Eq. 34 predicts a qualitatively similar behavior to the DNS simulation results. Quantitatively, Eq. 34 overpredicts all partially-densified surface areas. An increase in the Thiele modulus to an intermediate value $K = 0.01$ seems to alleviate some of this discrepancy at the expense of other discrepancies.

Models in Eq. 33 and 34 seem to roughly represent the limiting behavior with respect to Thiele modulus for all densified preform geometries shown in Fig. 17. Perhaps an exception is the Aligned case, where at $K = 0.1$, Eq. 34 does a better job of describing the densified surface area dependence on porosity. No DNS simulations were performed for $K > 0.1$.

The main conclusion from Fig. 17 is that the structure functions depend upon finite Thiele modulus effects. Thus, current semi-analytical formulations for them are not able to generally describe the CVI densification

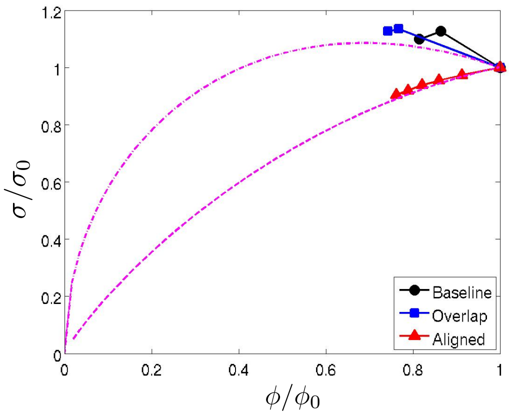

(a) ***K*** **= 0.1**

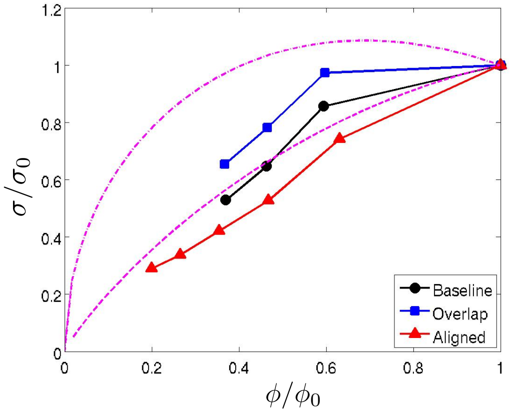

(b) ***K*** **= 0.01**

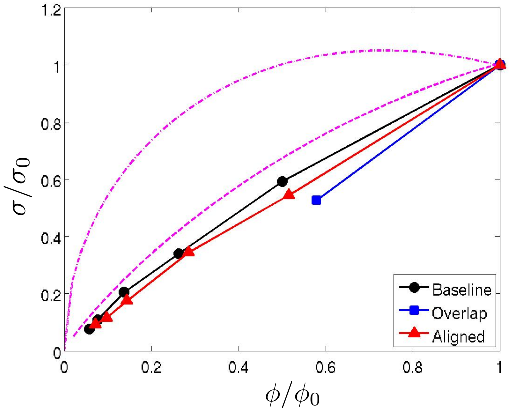

(c) ***K*** **= 0.001**

Figure 17. Deposited surface area dependence on porosity for decreasing Thiele moduli. Magenta lines in the figures are the analytical functions: Eq. 33 is given by the dash-dot lines, Eq. 34 by the dash-dash lines.

trends that have been simulated by the DNS. The DNS-based correlations of Fig. 17 can be used directly in the mean-field CFD simulations of fiber-woven porous media.

5.2 Modeling of flow infiltration

CVI CFD simulations which include woven preforms also require models to accurately describe the impact of the unresolved, evolving densification fronts on the transport of mass, momentum, and energy. A standard porous media model is given by

$$\begin{aligned} B &= \frac{1}{C_1}\frac{\phi^3}{\sigma^2} && \text{(35a)} \\ \mathcal{D}_{\text{eff},j} &= \frac{\phi}{C_2}\mathcal{D}_{j,\text{mix}} && \text{(35b)} \\ k_{\text{eff}} &= \phi k + (1-\phi)k_s \ , && \text{(35c)} \end{aligned}$$

where B is the permeability of the porous media, C_1 is the Kozeny-Carman constant, $\mathcal{D}_{\text{eff},j}$ is the effective diffusivity of the j-th species through the densifying preform, $\mathcal{D}_{j,\text{mix}}$ is the molecular (free) diffusivity, C_2 is the tortuosity parameter, k_{eff} is the effective conductivity, and k and k_s are the conductivities of the gas and solid, respectively. The “constants” C_1 and C_2 are application specific and are commonly made functions of the porous media geometry. That is, the scaling of the infiltration characteristics (B and $\mathcal{D}_{\text{eff},j}$) with ϕ, for example, is generally not known.

In the fiber-weave case, values for B and $\mathcal{D}_{\text{eff},j}$ are obtained experimentally. This is done by partially densifying the preform of interest via CVI processing, then employing an inert gas apparatus to flow test the partially-densified specimen. This approach can obviously become costly given the diversity of preform geometries and variety of partially-densified states. The number of experimental trials becomes particularly large if the scaling of the infiltration characteristics is to be accurately quantified.

The present DNS simulations provide a relatively inexpensive method to supplement such experimental investigations at a small fraction of the cost. Since the densified geometry is available at any given time from the level-set field, the partially-densified preform can be treated as any generic solid model for CFD simulations conventionally employed by industry, *i.e.*, using basic laminar flow calculations.

Employing the conventional CFD simulations, the permeability is computed from Darcy’s law:

$$\frac{\Delta p}{L} = -\frac{1}{B}\mu u_0 \ , \tag{36}$$

where Δp is the pressure loss across distance L due to the viscous fluid. The fluid has constant absolute viscosity μ and constant density. The massflow rate is fixed with initial velocity u_0 set in the through-thickness direction at the inflow boundary. Figure 18 shows an illustrative pressure field from such a calculation for a fixed preform geometry characterized by D, σ, and ϕ. Varying a fluid property or u_0 in Eq. 36 while keeping the geometry fixed, yields a linear relationship to directly compute the inverse of the permeability, $1/B$. The Reynolds number must be low in the CFD simulations to avoid the inertial losses neglected by Eq. 36.

Similarly, the effective diffusivity is computed by solving, for a fixed geometry, the binary Fickian diffusion problem illustrated in Fig. 19. At steady-state, the concentration gradients in the through-thickness

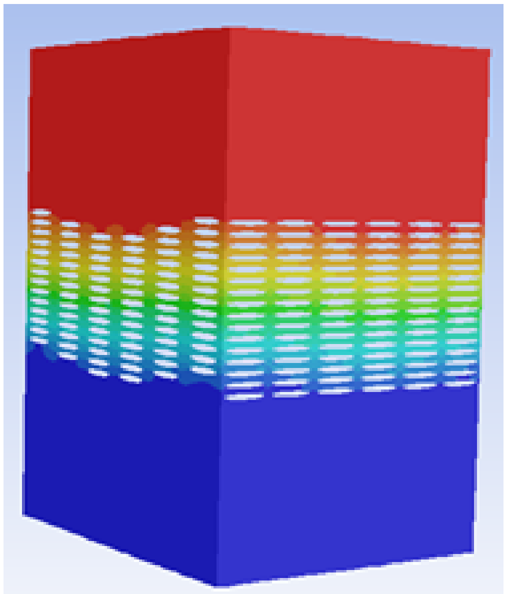

Figure 18. Steady-state pressure field used to compute weave permeability.

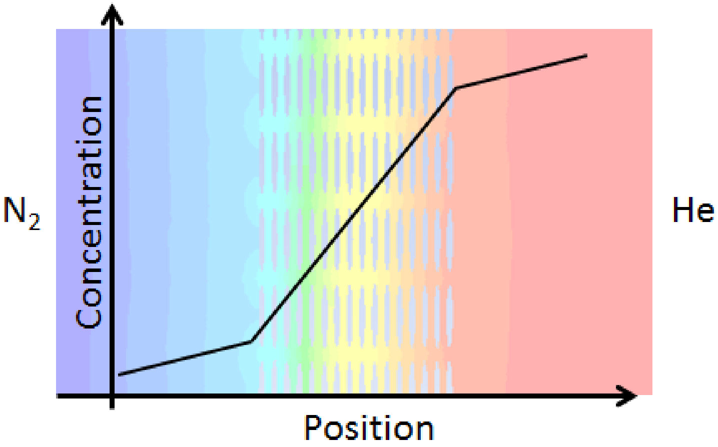
N2
Concentration
He
Position

Figure 19. Inert species concentrations used to compute effective diffusivity through the weave.

direction (dY_1/dz) of either inert gas becomes linear. Fick's first law, used to model the diffusive gas transport in the CFD, describes the mass flux as

$$J_j = -\mathcal{D}_{12}\frac{dY_j}{dz} \ , \tag{37}$$

where $\mathcal{D}_{12}$ is the constant binary diffusion coefficient. If we define an instance of Fick's law both inside ($J_{j,\mathrm{inside}} = \mathcal{D}_{\mathrm{eff}}(dY_j/dz)_{\mathrm{inside}}$) and outside ($J_{j,\mathrm{outside}} = \mathcal{D}_{12}(dY_j/dz)_{\mathrm{outside}}$) of the porous media and take advantage of the fact that the mass flux inside the porous media is equal to the max flux outside ($J_{j,\mathrm{inside}} = J_{j,\mathrm{outside}}$), the ratio of effective diffusivity to bulk diffusivity becomes equal to the ratio of concentration gradient outside the porous media to the gradient inside:

$$\frac{\mathcal{D}_{\mathrm{eff},j}}{\mathcal{D}_{12}} = \frac{(dY_j/dz)_{\mathrm{outside}}}{(dY_j/dz)_{\mathrm{inside}}} \ . \tag{38}$$

The CFD calculations are repeated for different partially-densified preform geometries to develop scaling relationships.

Figure 20 shows the permeabilities and effective diffusivities of the densified preforms at regular CVI processing time intervals up to the completion time, when the ultimate porosity has been reached. The three preform designs (Baseline, Overlap, and Aligned preform geometry configurations) are the same as those described in the discussion surrounding Fig. 17. In all cases shown in Fig. 20, the Thiele modulus is fixed at $K = 0.001$. For reference, the magenta dash-dash lines show ϕ scaling dependencies: $\sim \phi^3$ and ϕ^4 in Fig. 20 (a), and $\sim \phi^1$ and ϕ^2 in (b).

The commonly accepted scaling of the infiltration properties are

$$\sigma^2 B \sim \phi^3 \quad \text{and} \quad \frac{\mathcal{D}_{\mathrm{eff},j}}{\mathcal{D}_{12}} \sim \phi \ . \tag{39}$$

These relationships represent the well-known Kozeny-Carman scaling and form the basis of Eq. 35.

Focusing first on results from the Baseline preform (black circles in Fig. 20), an approximate scaling of $\sigma^2 B \sim \phi^m$ and $\mathcal{D}_{\mathrm{eff},j}/\mathcal{D}_{12} \sim \phi^n$ are observed with exponents m and n approximately independent of CVI processing time. However, the commonly accepted scaling exponents given by Eq. 39 underpredict the sensitivity to ϕ in both infiltration properties.

For the other preform geometries (Overlap and Aligned preform geometries), the standard scaling (Eq. 39) is not valid across the entire range of ϕ. Recall, the Overlap preform design represents a geometry with a higher tortuosity with respect to the Baseline, while the Aligned preform a lower tortuosity. The results of Fig. 20 say that a simple tortuosity correction (via parameters C_1 and C_2 in Eq. 35) could not be characterized by an additional ϕ dependence alone, as is commonly resorted to in practice.

An important trend to observe in Fig. 20 is the large range in infiltration characteristics of woven fiber preforms. At a fixed porosity, the permeability can vary by multiple orders-of-magnitude, with the Aligned geometry showing the highest permeability. A relatively large variation is observed in the effective diffusivity as well, with again the Aligned ply preform exhibiting the largest effective diffusivity. Further, while both infiltration characteristics appear to have complex scaling properties, the trends between the two are similar. Figure 21 highlights this latter observation, which shows the direct proportionality between B and $\mathcal{D}_{\mathrm{eff},j}$:

$$\sigma^2 B \sim \left(\frac{\mathcal{D}_{\mathrm{eff},j}}{\mathcal{D}_{12}}\right)^p \ . \tag{40}$$

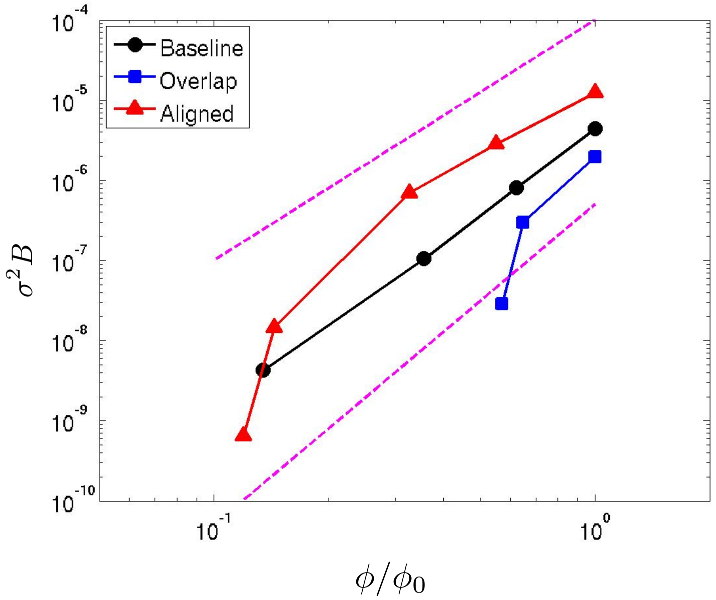

(a) Permeability

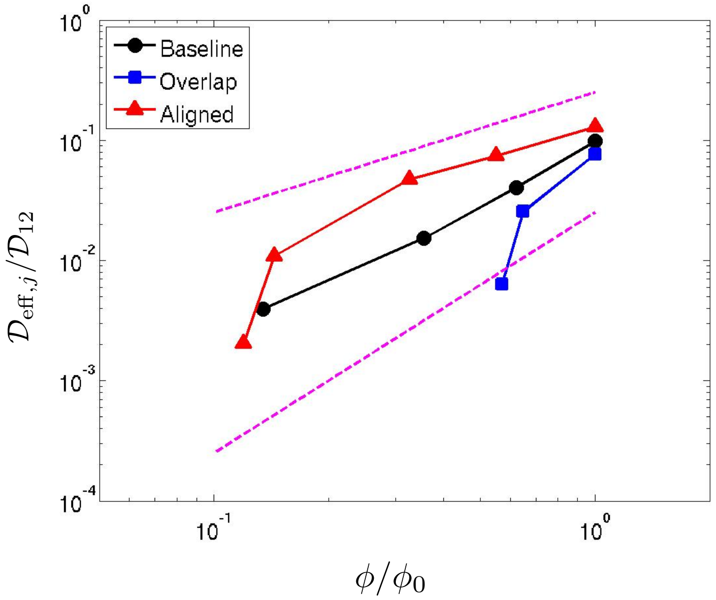

(b) Effective Diffusivity

Figure 20. Permeability and effective diffusivity scaling with porosity for the three different preform geometries.

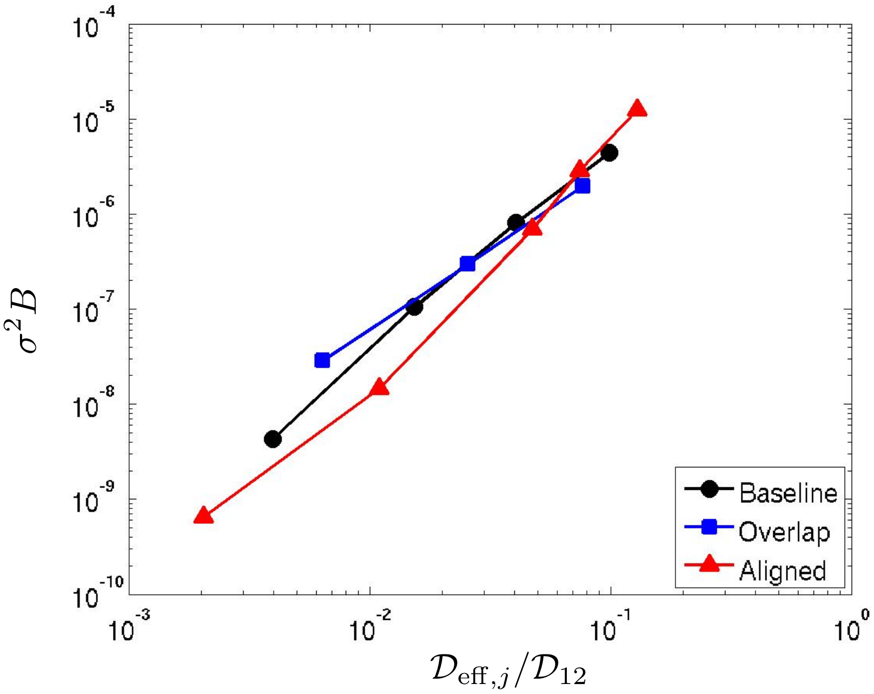

Figure 21. Proportionality of permeability to effective diffusivity.

Here, $p = 2.40$ (computed in the least-squares sense for the Aligned case), $p = 2.16$ (Baseline), and $p = 1.70$ (Overlap). The sensitivity decreases with increasing tortuosity of the preform geometries considered in the present study.

6. FUTURE WORK

Two key physical deficiencies in the virtual (numerical) experiments have been recognized:

1. Lack of bulk or convective flow effects (in the current work, the unsteady transport of reactants was governed by diffusion only), and
2. Lack of realistic SiC deposition kinetics (in the current work, only a global, one-step kinetic model was employed).

With regard to item 1, experiments carried out at ORNL in the 1990s were able to demonstrate a reduction of CVI processing times from months to hours using “forced-flow” or convection assisted methods. At a production level, this would represent a monumental advancement for the CVI processing industry. The proposed enhancements to the toolset will allow the current optimizations to include forced-flow CVI processing techniques. With regard to item 2 above, methyltrichlorosilane (MTS) with a hydrogen gas carrier are the industry standard reagents for CVI manufacturing applications. At practical CVI processing conditions, it is well-known that the SiC precursors are produced through multiple kinetic pathways [33] and compete with other key reactions [34, 35] to deposit the SiC matrix. Incorporation of the multiple scalar transport and reaction timescales will make the current model physically accurate and thereby enable the optimizations to make quantitative predictions rather than only predict trends. A primary objective of the future work will be to add the above two new capabilities to the already developed toolset.

References

[1] G. Tryggvason, B. Bunner, A. Esmaeeli, D. Juric, N. Al-Rawahi, W. Tauber, J. Han, S. Nas, and Y. J. Jan. A Front-Tracking Method for the Computations of Multiphase Flow. *Journal of Computational Physics*, 169(2):708–759, May 2001.

[2] W. Bo, X. Liu, J. Glimm, and X. Li. A Robust Front Tracking Method: Verification and Application to Simulation of the Primary Breakup of a Liquid Jet. *SIAM Journal on Scientific Computing*, 33(4):1505–1524, January 2011.

[3] C. W Hirt and B. D Nichols. Volume of fluid (VOF) method for the dynamics of free boundaries. *Journal of Computational Physics*, 39(1):201–225, January 1981.

[4] Gunduz Caginalp. An analysis of a phase field model of a free boundary. *Archive for Rational Mechanics and Analysis*, 92(3):205–245, September 1986.

[5] Ryo Kobayashi. Modeling and numerical simulations of dendritic crystal growth. *Physica D: Nonlinear Phenomena*, 63(3):410–423, March 1993.

[6] Mark Sussman, Peter Smereka, and Stanley Osher. A Level Set Approach for Computing Solutions to Incompressible Two-Phase Flow. *Journal of Computational Physics*, 114(1):146–159, September 1994.

[7] Javed Shaikh, Atul Sharma, and Rajneesh Bhardwaj. On sharp-interface level-set method for heat and/or mass transfer induced Stefan problem. *International Journal of Heat and Mass Transfer*, 96:458–473, May 2016.

[8] Frédéric Gibou, Ronald Fedkiw, Russel Caflisch, and Stanley Osher. A Level Set Approach for the Numerical Simulation of Dendritic Growth. *Journal of Scientific Computing*, 19(1-3):183–199, December 2003.

[9] Shi Jin, Xuelei Wang, Thomas L. Starr, and Xinfu Chen. Robust Numerical Simulation of Porosity Evolution in Chemical Vapor Infiltration I: Two Space Dimension. *Journal of Computational Physics*, 162(2):467–482, August 2000.

[10] J. A. Sethian. *Level Set Methods and Fast Marching Methods: Evolving Interfaces in Computational Geometry, Fluid Mechanics, Computer Vision, and Materials Science*. Cambridge University Press, June 1999.

[11] Mathieu Coquerelle and Stéphane Glockner. A fourth-order accurate curvature computation in a level set framework for two-phase flows subjected to surface tension forces. *Journal of Computational Physics*, 305:838–876, January 2016.

[12] Frederic Gibou, Ronald Fedkiw, and Stanley Osher. A review of level-set methods and some recent applications. *Journal of Computational Physics*, 353:82–109, January 2018.

[13] J. A. Sethian. A fast marching level set method for monotonically advancing fronts. *Proceedings of the National Academy of Sciences*, 93(4):1591–1595, February 1996.

[14] Hongkai Zhao. A fast sweeping method for Eikonal equations. *Mathematics of Computation*, 74(250):603–627, 2005.

[15] Hongkai Zhao. Parallel implementation of the fast sweeping method. *International Journal of Computer Mathematics - IJCM*, 25, January 2006.

[16] Jianliang Qian, Yong-Tao Zhang, and Hong-Kai Zhao. A fast sweeping method for static convex Hamilton-Jacobi equations. *Journal of Scientific Computing*, 31(1):237–271, 2007.

[17] Yong-Tao Zhang, Hong-Kai Zhao, and Jianliang Qian. High Order Fast Sweeping Methods for Static HamiltonâĂŞJacobi Equations. *Journal of Scientific Computing*, 29(1):25–56, October 2006.

[18] Y.-T. Zhang and C.-W. Shu. Chapter 5 - ENO and WENO schemes. In Rémi Abgrall and Chi-Wang Shu, editors, *Handbook of Numerical Methods for Hyperbolic Problems*, volume 17 of *Handbook of Numerical Analysis*, pages 103 – 122. Elsevier, 2016.

[19] D. Chopp. Some Improvements of the Fast Marching Method. *SIAM Journal on Scientific Computing*, 23(1):230–244, January 2001.

[20] Stanley Osher and James A Sethian. Fronts propagating with curvature-dependent speed: Algorithms based on Hamilton-Jacobi formulations. *Journal of Computational Physics*, 79(1):12–49, November 1988.

[21] Olivier Desjardins, Vincent Moureau, and Heinz Pitsch. An accurate conservative level set/ghost fluid method for simulating turbulent atomization. *Journal of Computational Physics*, 227(18):8395–8416, September 2008.

[22] R. Mittal, H. Dong, M. Bozkurttas, F. M. Najjar, A. Vargas, and A. von Loebbecke. A versatile sharp interface immersed boundary method for incompressible flows with complex boundaries. *Journal of Computational Physics*, 227(10):4825–4852, May 2008.

[23] Yousef Saad. *Iterative methods for sparse linear systems*, volume 82. Society for Industrial and Applied Mathematics, 2003.

[24] Loyce M Adams. Iterative algorithms for large sparse linear systems on parallel computers. Technical report, NASA, Langley Research Center, Hampton, Virginia, 1982.

[25] T.L. Starr. Gas transport model for chemical vapor infiltration. *J. Mater. Res.*, 10(9):2360–2366, 1995.

[26] J. Y. Ofori and S. V. Sotirchos. Structural model effects on the predictions of chemical vapor infiltration models. *J. Electrochem. Soc.*, 143(6):1962–1973, 1996.

[27] G.-Y. Chung and B. J. McCoy. Modeling of chemical vapor infiltration for ceramic composites reinforced with layered, woven fabrics. *J. Am. Ceram. Soc.*, 74(4):746–751, 1991.

[28] G.-Y. Chung, B. J. McCoy, J. M. Smith, and D. E. Cagliostro. Chemical vapor infiltration: Dispersed and graded depositions for ceramic composites. *AIChE J.*, 39(11):1834–1846, 1993.

[29] R. P. Currier, D. J. Devlin, and J. Morzinski. Dynamics of chemical vapor infiltration in carbon fiber bundles. *J. Adv. Matl.*, X:13–24, 1996.

[30] B. W. Sheldon and T. M. Besmann. Reaction and diffusion kinetics during the initial stages of isothermal chemical vapor infiltration. *J. Am. Ceram. Soc.*, 74(12):3046–53, 1991.

[31] K. Guan, L. Cheng, Q. Zeng, Z.-Q. Feng, L. Zhang, H. Li, and H. Ren. Modeling of pore structure

evolution within fiber bundle during chemical vapor infiltration process. *Chem. Engr. Sci.*, 66:5852–61, 2011.

[32] K. Guan, L. Cheng, Q. Zeng, L. Zhang, J. Deng, K. Li, and H. Li. Modeling of pore structure evolution between bundles of plain woven fabrics during chemical vapor infiltration process: The influence of preform geometry. *J. Am. Ceram. Soc.*, 96(1):51–61, 2013.

[33] Yingbin Ge, Mark S. Gordon, Francine Battaglia, and Rodney O. Fox. Theoretical Study of the Pyrolysis of Methyltrichlorosilane in the Gas Phase. 3. Reaction Rate Constant Calculations. *The Journal of Physical Chemistry A*, 114(6):2384–2392, February 2010.

[34] F. Loumagne, F. Langlais, and R. Naslain. Experimental kinetic study of the chemical vapour deposition of SiC-based ceramics from CH3SiCl3H2 gas precursor. *Journal of Crystal Growth*, 155(3):198–204, October 1995.

[35] George D. Papasouliotis and Stratis V. Sotirchos. On the Homogeneous Chemistry of the Thermal Decomposition of Methyltrichlorosilane. *Journal of The Electrochemical Society*, 141(6):1599, 1994.